Benchmarking numerical simulation of induced fault slip with semi-analytical solutions

Novikov, Aleksei; Shokrollahzadeh Behbahani, Sara; Voskov, Denis; Hajibeygi, Hadi; Jansen, Jan Dirk

DOI
10.1007/s40948-024-00896-1

Publication date
2024

Document Version
Final published version

Published in
Geomechanics and Geophysics for Geo-Energy and Geo-Resources

Citation (APA)
Novikov, A., Shokrollahzadeh Behbahani, S., Voskov, D., Hajibeygi, H., & Jansen, J. D. (2024). Benchmarking numerical simulation of induced fault slip with semi-analytical solutions. *Geomechanics and Geophysics for Geo-Energy and Geo-Resources*, *10*(1), Article 182. https://doi.org/10.1007/s40948-024-00896-1

Geomech. Geophys. Geo-energ. Geo-resour. (2024) 10:182
https://doi.org/10.1007/s40948-024-00896-1

RESEARCH

Benchmarking numerical simulation of induced fault slip with semi-analytical solutions

Aleksei Novikov · Sara Shokrollahzadeh Behbahani · Denis Voskov · Hadi Hajibeygi · Jan-Dirk Jansen

Received: 5 March 2024 / Accepted: 18 October 2024

Abstract Pore pressure fluctuation in subsurface reservoirs and its resulting mechanical response can cause fault reactivation. Numerical simulation of such induced seismicity is important to develop reliable seismic hazard and risk assessments. However, modeling of fault reactivation is quite challenging, especially in the case of displaced faults, i.e., faults with non-zero offset. In this paper, we perform a systematic benchmarking study to validate two recently developed numerical methods for fault slip simulation. Reference solutions are based on a semi-analytical approach that makes use of inclusion theory and Cauchy-type singular integral equations. The two numerical methods both use finite volume discretizations, but they employ different approaches to represent faults. One of them uses a conformal discrete fault model (DFM) while the other employs an embedded (non-conformal) fault model. The semi-analytical test cases cover a vertical frictionless fault, and inclined displaced faults with constant friction and slip-weakening friction. It was found that both numerical methods accurately represent pre-slip stress fields caused by pore pressure changes. Moreover, they also successfully cope with a vertical frictionless fault. However, for the case with an inclined displaced fault with a constant friction coefficient, the embedded method can not converge for the post-slip phase, whereas the DFM successfully coped with both constant and slip-weakening friction coefficients. In its current implementation, the DFM is therefore the model of choice when accurate simulation of local faulted systems is required.

Article Highlights

- A series of benchmarks of increasing complexity is designed to facilitate rigorous validation of the induced fault slip simulations, particularly in challenging displaced fault configuration.
- The validation of Finite-Volume-based simulators reveals substantially higher accuracy provided by the conformal discrete fault model compared to the embedded discrete fault model.

A. Novikov (✉) · S. Shokrollahzadeh Behbahani · D. Voskov · H. Hajibeygi · J.-D. Jansen
Department of Geoscience and Engineering, Delft University of Technology (TU Delft), Stevinweg 1, 2628 CN Delft, The Netherlands
e-mail: a.novikov@tudelft.nl

S. Shokrollahzadeh Behbahani
e-mail: s.shokrollahzadehbehbahani@tudelft.nl

D. Voskov
e-mail: d.v.voskov@tudelft.nl

H. Hajibeygi
e-mail: h.hajibeygi@tudelft.nl

J.-D. Jansen
e-mail: j.d.jansen@tudelft.nl

D. Voskov
Department of Energy Science and Engineering, Stanford University, 367 Panama Street, Stanford, CA 94305, USA

Keywords Induced seismicity · Semi-analytical solution · Discrete fault modeling · Finite-volume method · Embedded discrete formulation · Conformal discrete formulation · Displaced fault · Fault offset · Fault reactivation · Nucleation

1 Introduction

1.1 Induced seismicity

Safe and sustainable exploitation of geo-energy resources requires accurate assessments of the associated risks, including the risk of induced seismicity. Seismic events can result from the reactivation of natural faults due to subsurface engineering activities. Numerous anthropogenic activities have been identified as potential triggers of these seismic events: reservoir impoundment (Carder 1945; Gupta 2002), fluid withdrawal (Segall 1989; Van Thienen-Visser and Breunese 2015; Muntendam-Bos et al. 2022), fluid injection (Healy et al. 1968; Davis and Pennington 1989; Kim 2013), hydraulic fracturing (Atkinson et al. 2016; Schultz et al. 2017), mining (Riemer and Durrheim 2012), geothermal energy production (Majer et al. 2007; Ellsworth et al. 2019; Buijze et al. 2020) and CO2 geological storage (Cheng et al. 2023). Notably, an abrupt rise in the rate of induced seismicity has been observed around the globe since 2008 (Keranen and Weingarten 2018). The risks associated with induced seismicity stem from the potential for structural damage and adverse effects on the environment and human life. These concerns have been documented in several studies that highlight the importance of hazard and risk assessments and operational strategies for subsurface activities (McGarr et al. 2002; Voort and Vanclay 2015; Elk et al. 2017).

1.2 Numerical simulation

The increasing number of induced earthquakes has led to the development of various numerical models for fault reactivation. Classically, the Galerkin finite element method (FEM) has been employed to investigate the onset of induced fault slip for different geo-energy applications (Jha and Juanes 2014; Garipov et al. 2016; Garipov and Hui 2019; Franceschini et al. 2022). Additionally, methods such as the Embedded Finite Element Method (EFEM) (Cusini et al. 2021) and the extended Finite Element Method (XFEM) (Xu et al. 2021; Han and Younis 2023) have demonstrated their efficacy in the modeling of fault reactivation. Recently, Finite Volume Methods (FVMs) have also gained considerable interest in the computational geoscience community, where they have been preferred over the FEM due to their local mass conservation for simulation of nonlinear transport equations. The corresponding numerical schemes for staggered (Deb and Jenny 2017; Sokolova et al. 2019) and collocated (Nordbotten 2014; Berge et al. 2020; Terekhov 2020; Tripuraneni et al. 2023) grids have been developed and successfully utilized for the investigation of induced fault slip (Keilegavlen et al. 2021; Shokrollahzadeh Behbahani et al. 2022; Novikov et al. 2022b). The advantages of the FVM include the local preservation of momentum balance, discontinuous basis functions (potentially beneficial for resolving explicit faults), and seamless integration with fluid mass and energy balance solvers.

1.3 Fault models

Along with numerical methods, fault representation in a computational grid is pivotal for an accurate evaluation of the stress state around discontinuities. The Discrete Fracture Model (DFM) implies that fault partitioning is conformal with domain partitioning while the Embedded Discrete Fracture Model (EDFM) allows the two grids to be independent. Both models have been applied for the modeling of induced seismicity (Keilegavlen et al. 2021; Franceschini et al. 2022; Novikov et al. 2022b; Deb and Jenny 2017; Cusini et al. 2021; Shokrollahzadeh Behbahani et al. 2022).

Nevertheless, the numerical modeling of fault reactivation represents a challenging task that requires rigorous validation. Contact mechanics requires special attention due to the inequality constraints it imposes and friction laws that strongly affect the occurrence of seismicity. Additionally, the reservoir geometry can significantly affect the potential for fault reactivation and seismicity. For instance, compartmentalized formations often exhibit discontinuities, such as displaced faults, i.e. faults with a non-zero offset, that require an accurate representation. Given the same computational grid, distinct numerical methods may yield divergent results around these discontinuities, adding complexity to the seismic hazard assessment of real-world geological configurations.

1.4 (Semi-)analytical solutions

In the absence of detailed field data, the validation of numerical models can be done with the help of analytical and semi-analytical solutions. Closed-form analytical expressions for the poroelastic stresses in a reservoir undergoing depletion or injection can be obtained with the aid of inclusion theory (Eshelby 1957), or the closely-related nucleus of strain concept (Geertsma 1966, 1973), based on potential theory (Goodier 1937). These methods have initially been used to estimate subsidence and stress fields outside subsurface reservoirs (Geertsma 1973; Segall 1985, 1989, 1992; Segall et al. 1994). Stresses inside an elliptical reservoir were subsequently considered by Segall and Fitzgerald (1998) and inside rectangular reservoirs by Soltanzadeh and Hawkes (2008). Expressions for induced stresses in a reservoir with a displaced fault, undergoing quasi-steady state depletion or injection, were published by Jansen et al. (2019). Similar expression were presented concurrently by Lehner (2019) and later by Wu et al. (2021, 2024), while a further clarification of some underlying mathematical aspects can be found in Cornelissen et al. (2024). In case of a non-homogeneous pressure field, inclusion theory can still be applied to obtain the fault stresses but the resulting integrals have to be solved numerically; see Cornelissen and Jansen (2023) for an example and further references.

The representation of faults in the form of dislocations (Hills et al. 1996; Weertman 1996) simplifies the problem of pressure-induced fault slip to a Cauchy integral equation over the fault, which can subsequently be solved semi-analytically using Chebyshev polynomials (Mavko 1982; Segall 2010; Jansen and Meulenbroek 2022) or Gauss-Chebyshev quadrature (Hills et al. 1996; Viesca and Garagash 2018; Meulenbroek and Jansen 2024).

1.5 Comparison

This paper provides a series of semi-analytical solutions of increasing complexity, as listed in Table 1, for rigorous validation of computational geomechanics engines in challenging settings. In particular these solutions can be used to validate numerical schemes for the simulation of frictional contact in the presence of both strong and weak discontinuities (i.e. discontinuities in displacements and stresses respectively). We demonstrate the use of this series of semi-analytical solutions by examining the capacities of two novel poromechanical simulation approaches based on the FVM. The first one, inspired by earlier work of Garipov et al. (2016) and further developed and implemented by Novikov et al. (2022b), employs a discrete fault model (DFM). It forms part of a comprehensive porous media simulator, the Delft Advanced Reservoir Terra Simulator (DARTS), and will be referred to with that acronym. The second approach, inspired by an earlier study of Deb and Jenny (2017) and further developed by Shokrollahzadeh Behbahani et al. (2022), uses a smoothed embedded discrete fault model (sEFVM) and will be referred to with that last acronym. Both methods are developed and implemented as part of the *DeepNL Science4Steer* project (NWO 2022). Appendices 1 and 2 provide a brief overview of their characteristic features. Moreover, the computational grids used in this study are presented in Appendix 3.

The comparison is performed against semi-analytical solutions for pre-slip fault stresses and the resulting induced fault slip. These solutions have been developed using inclusion theory and Cauchy singular integral equations with details reported earlier in Jansen et al. (2019); Jansen and Meulenbroek (2022); Cornelissen et al. (2024) and Meulenbroek and Jansen (2024). Appendix 4 gives a brief overview of these methods. The semi-analytical benchmark data used to generate the figures in this paper are available in the form of an Excel file uploaded to the 4TU Data Repository: https://doi.org/10.4121/d77f1a2c-29ea-4572-ad72-e33ed8dc8d22.

Table 1 List of proposed benchmarks

Benchmark no.	Fault	Friction	Section
#0	–	–	2.4
#1	Vertical	Frictionless	3
#2	Inclined	Constant	4.1
#3	Inclined	Slip-weakening	4.2

Benchmark #0 represents the comparison of initial stresses while benchmarks #1 – #3 include the validation of fault responses caused by a pore pressure change

1.6 Notation

We employ the solid mechanics sign convention, i.e., positive strains and stresses imply extension and tension, respectively. Pore pressures are taken as positive. We will frequently refer to *inital* and *incremental* variables. Initial variables represent the state of the system before the start of reservoir depletion and are indicated with lowercase letters with superscript 0. Incremental variables represent the state of the system during reservoir depletion and are indicated with plain lowercase letters. The sums of initial and incremental variables are referred to as *combined* variables and they are indicated with capital letters. In particular, we have

$$\Sigma = \sigma^0 + \sigma, \quad P = p^0 + p, \tag{1}$$

to indicate combined stresses and pressures, respectively. Moreover, a common notation for *total* stresses σ and *effective* stresses σ' is applied. They are related to each other according to

$$\sigma' = \sigma + \alpha p, \quad \sigma'^0 = \sigma^0 + \alpha p^0, \quad \Sigma' = \Sigma + \alpha P, \tag{2}$$

where α is the Biot coefficient (Wang 2000).

1.7 Organization of the paper

This paper is organized as follows. In Sect. 2 we present the model setup used in our benchmark study and calculations for the unperturbed stress state. In Sect. 3 we consider a vertical frictionless displaced fault perturbed by depletion pressure, and compare numerical and semi-analytical solutions for the induced fault slip. Section 4 is devoted to the comparison of numerical and semi-analytical results in the case of an inclined displaced fault governed by static and slip-weakening friction laws. The paper is concluded in Sect. 5. The two finite volume strategies used in this benchmark study, including the formulation of the conformal and embedded fracture models, are described in Appendices 1 and 2. Moreover, Appendix 3 provides an overview of computational grids used in numerical calculations. A brief description of the semi-analytical techniques is presented in Appendix 4.

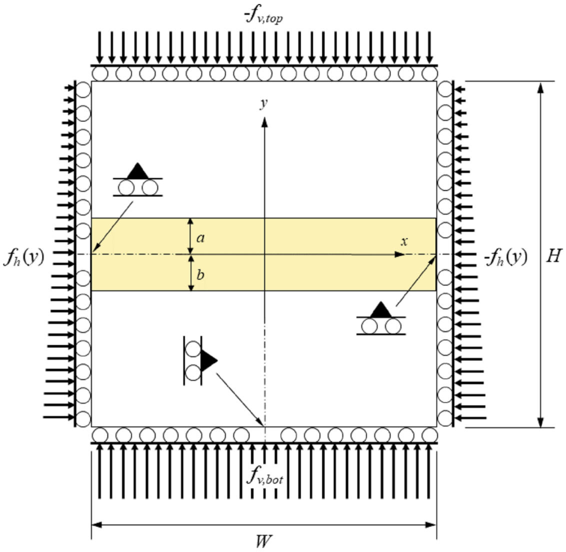

Fig. 1 Simulation set-up to represent a square reservoir without faults (not to scale). Load configuration and mechanical boundary conditions to simulate initial stresses

2 Depletion in a reservoir without faults

2.1 Model

Consider a schematic representation of a simulation domain to model a homogeneous horizontal reservoir with part of the overburden and underburden and without faults, as shown in Fig. 1. The simulation domain is a square with the origin of the coordinate system placed at the center of the domain. We consider quasi-steady-state poromechanics in a domain with uniform elastic properties. In that case, there is no need to solve for the pressure field which, instead, can be specified in each cell a-priori. Moreover, it is assumed that no incremental pressure change will occur in the overburden and underburden. The incremental reservoir pressure, as occurs during depletion, can therefore be simulated by specifying the pressure in the reservoir cells while keeping the pressures in the overburden and underburden equal to their initial values. Alternatively, these burdens may be represented as consisting of a purely elastic solid without porosity.

Figure 1 indicates the horizontal and vertical load configuration and the mechanical boundary conditions to simulate the initial stress field. The dimensions of the simulation domain and the reservoir are indicated in Table 2, with $a = b = 112.5$ m, together with several other parameters that will be of relevance for later steps of the code comparison exercise. Uniform vertical distributed loads, with different magnitudes and opposite directions, are applied from the top and bottom boundaries, while non-uniform horizontal distributed loads, with equal magnitudes but opposite directions, are applied from both sides, thus ensuring a stress field that is symmetric around the *y* axis. To constrain rigid body translations and rotation, horizontal displacement is constrained in a single point at the bottom center while vertical displacement is constrained in two discrete points at the left and right boundaries. In all other points at the boundaries, the shear stresses are set equal to zero, as indicated by the 'rollers' at all sides. This configuration, with a minimum number of constraints at the boundaries, ensures that during the initial loading no spurious shear stresses are developed because of restricted displacements. Further details of the initial stress field are given in the next section. After the simulation of these initial stresses, all vertical displacements are shifted such that the reference (zero vertical displacement) is located at the bottom of the simulation domain.

To enable the subsequent simulation of the depletion process in the reservoir, the vertical boundary conditions are changed to roller-type ones with fixed horizontal displacements, and the bottom one to a roller-type condition with fixed vertical displacements, see Fig. 2. The three constraints at the bottom and the sides are removed. Together with the use of plane-strain conditions in the simulation codes, which can be interpreted as fixing the horizontal displacements in the *z* direction, and given the horizontally constant geometry of the reservoir layer, the simulation domain approximates an infinite horizontal reservoir in *x* and *z* directions.

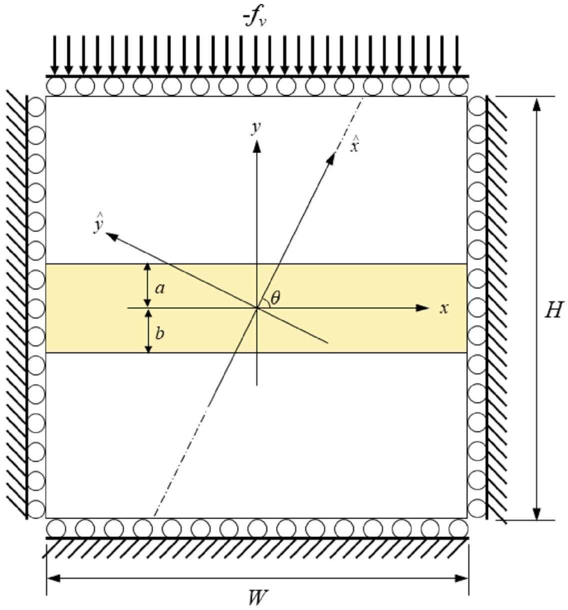

Fig. 2 Identical to Fig. 1 but now with load configuration and mechanical boundary conditions to simulate incremental stresses. The figure also shows a line through the center at an angle of $\theta = 70$ degrees with respect to horizontal, with an associated rotated $\hat{x} - \hat{y}$ coordinate system

2.2 Initial stresses

With the center of the reservoir (and therefore the center of the simulation domain) at a depth of 3500 m and a height of the simulation domain of 4500 m it follows that the top of the domain is at 1250 m below the surface and 2250 m above the center. The required vertical distributed load $f_{v,top}$ to simulate the combined rock and fluid weight of the overburden at that depth follows from the text at the bottom of Table 2 as

$$\begin{aligned} f_{v,top} = {} & \sigma^0_{yy}(2250) = [(1-\phi)\rho_s + \phi\rho_{fl}] \\ & g(y - D_0) = -29.50e6 \text{ Pa}, \end{aligned} \tag{3}$$

where ϕ is porosity, ρ_s is solid density, ρ_{fl} is fluid density, g is acceleration of gravity, and D_0 is depth below the surface at the vertical center of the reservoir. Because compressive normal stresses are negative, $f_{v,top}$ is also negatively valued which implies that it acts in the negative y direction (i.e., downward, as indicated in Fig. 1.) The distributed load at the bottom of the domain is obtained in the same manner as

$$f_{v,bot} = -\sigma^0_{yy}(-2250) = 135.7e6 \text{ Pa}, \tag{4}$$

which, in line with its positive value, acts upward. The required horizontal distributed load f_h can be obtained as

$$f_h(y) = -\sigma^0_{xx}(y) = -\left\{K^0[\sigma^0_{yy}(y) + \alpha p^0(y)] - \alpha p^0(y)\right\}, \tag{5}$$

where K^0 is the ratio of initial effective horizontal to vertical stresses. Because the initial fluid pressures

Table 2 Reservoir properties, fault geometry and simulation domain

Symbol	Property	Value	Units
a	See Figs. 1 and 2	112.5 or 75	m
b	"	112.5 or 150	m
D_0	Depth at reservoir center ($y = 0$)	3500	m
g	Acceleration of gravity	9.81	m/s^2
G	Shear modulus	6500	MPa
H	Height of simulation domain	4500	m
K^0	Ratio of initial effective horizontal to vertical stresses	0.5	–
p	Incremental reservoir pressure	–25	MPa
p_0^0	Initial reservoir pressure at reservoir center	35	MPa
W	Width of simulation domain	4500	m
α	Biot coefficient	0.9	–
β	Effective stress coefficient for fault friction	0.9	–
θ	Dip angle	90 or 70	deg
κ	Cohesion	0	MPa
μ	friction coefficient	0.52	–
ν	Poisson's coefficient	0.15	–
ρ_{fl}	Fluid density	1020	kg/m^3
ρ_s	Solid density	2650	kg/m^3
ϕ	Porosity	0.15	–

The initial vertical stress, initial pressure and initial effective normal stress have been computed as: $\sigma_{yy}^0(y) = [(1-\phi)\rho_s + \phi\rho_{fl}]g(y - D_0)$, where $\sigma_v^0 < 0$, $p^0(y) = p_0^0 - \rho_{fl}\, g\, y$, $\sigma_\perp'^0(y) = \sigma_\perp^0(y) + \alpha p^0(y)$.

at the top and bottom of the simulation domain are given by

$$\begin{aligned} p^0(2250) &= p_0^0 - \rho_{fl}\, g\, y = 12.49e6 \text{ Pa}, \\ p^0(-2250) &= 57.51e6 \text{ Pa}, \end{aligned} \tag{6}$$

where p_0^0 is the initial reservoir pressure at depth D_0, the values of f_h at the top and bottom of the domain follow as

$$f_h(2250) = 20.37e6 \text{ Pa}, \quad f_h(-2250) = 93.73e6 \text{ Pa}, \tag{7}$$

where the positive values of f_h imply that they act in the positive x direction, i.e., to the right, as indicated at the left boundary in Fig. 1. A distributed load $-f_h$, with an identical magnitude but acting in the negative x direction, is applied at the right boundary. The corresponding initial stress and pressure fields are given by

$$\begin{aligned} \sigma_{xx}^0(y) &= -57.05e6 + 16.30e3 \times y \text{ Pa}, \\ \sigma_{yy}^0(y) &= -82.60e6 + 23.60e3 \times y \text{ Pa}, \\ p^0(y) &= 35.00e6 - 10.06e3 \times y \text{ Pa}. \end{aligned} \tag{8}$$

Note that the initial shear stresses σ_{xy}^0 are zero by design.

2.3 Incremental stresses

After computation of the initial stresses, removal of the three constrained displacements, and fixing of horizontal displacements at the vertical boundaries and vertical displacements at the bottom, depletion can be simulated by adding a (negative) incremental pressure p to the cells in the reservoir. As indicated in Table 2, the standard depletion in our series of examples is $-25e6$ Pa.

2.4 Results

The application of distributed loads $f_{v,top}$, $f_{v,bot}$ and $\pm f_h$ to the boundaries, in order to compute the initial stress field, leads to initial vertical and horizontal displacements $u_y^0(x, y)$ and $u_x^0(x, y)$. We can use the constitutive equations for poroelastic plane strain to approximately compute $u_y^0(y)$, i.e., independent of x, at the top boundary (Wang 2000, Eq. 7.3). Assuming that the reference level of zero vertical displacements has been relocated to the bottom of the simulation domain (at $y = -2250$ m) this results in

$$\begin{aligned} u_y^0(2250) &= \int_{-\frac{H}{2}}^{\frac{H}{2}} \epsilon_{yy}^0 \, dy \\ &= \frac{1}{E}\int_{-\frac{H}{2}}^{\frac{H}{2}} \Big((1-\nu^2)\sigma_{yy}^0(y) - \nu(1+\nu)\sigma_{xx}^0(y) \\ &\quad + \alpha(1+\nu)(1-2\nu)p^0(y) \Big)\, dy = -13.66 \text{ m}, \end{aligned} \tag{9}$$

where H is the height of the simulation domain and E is Young's modulus which is computed from the shear modulus G and Poisson's ratio ν as $E = 2G(1+\nu) = 15.0e9$ Pa. We note that this large vertical displacement is due to vertical stresses caused by gravity forces, including those in the overburden. The corresponding vertical strain in the reservoir is less than 0.005 which is a reasonable value. The approximate initial horizontal displacements at the top left and bottom left of the simulation domain follow as (Wang 2000, Eq. 7.2)

$$\begin{aligned} u_x^0(-2250, 2250) &= -\int_{-\frac{W}{2}}^{0} \epsilon_{xx}^0(2250)\, dx \\ &= -\frac{W}{2}\epsilon_{xx}^0(2250) = 0.87 \text{ m}, \\ u_x^0(-2250, -2250) &= 3.98 \text{ m}, \end{aligned} \tag{10}$$

where we used

$$\begin{aligned} \epsilon_{xx}^0(y) = -\frac{W}{2E}[(1-\nu^2)\sigma_{xx}^0(y) - \nu(1+\nu)\sigma_{yy}^0(y) \\ + \alpha(1+\nu)(1-2\nu)p^0(y)], \end{aligned} \tag{11}$$

and where W is the width of the simulation domain. Identical displacements, but in opposite direction occur at the right boundary. The true displacement field will show small deviations from these approximate values because of contraction effects due to non-isotropic compression of the simulation domain as a result of the nonuniform initial distributed loads. However, the initial displacement field is not relevant for the subsequent steps in the comparison, as opposed to the initial stress field which is important because it determines the initial Coulomb stresses at the faults which will be considered later on.

As a reference for a future inclined fault configuration, consider a line through the center at an angle $\theta = 70$ deg. with respect to horizontal, see Fig. 2. The normal and shear stresses along this line can be computed as (Jansen and Meulenbroek 2022, Eqs. 2 and 3)

$$\begin{aligned} \sigma_\perp^0(y) &= \sigma_{\hat{y}\hat{y}}^0(y) = \sigma_{xx}^0(y)\sin^2\theta + \sigma_{yy}^0(y)\cos^2\theta \\ &= -60.04e6 + 17.15e3 \times y \text{ Pa}, \\ \sigma_\parallel^0(y) &= -\sigma_{\hat{x}\hat{y}}^0(y) = (\sigma_{xx}^0(y) - \sigma_{yy}^0(y))\sin\theta\cos\theta \\ &= 8.21e6 - 2.35e3 \times y \text{ Pa}, \end{aligned} \tag{12}$$

where $\hat{x}$ and $\hat{y}$ are co-rotated coordinates. The sign convention of the shear stresses $\sigma_\parallel$ has been chosen such that positive shear stresses indicate a normal faulting tendency, i.e. tendency for the right block to shift upward with respect to the left block.

Figure 3 displays the initial normal stresses and shear stresses along the inclined line for the two simulation codes and the analytical solution. Both codes produce a fully satisfactory match although the DARTS results for the shear stresses display small irregularities resulting from the use of an unstructured grid.

After changing the boundary conditions to fix the initial stress field, reservoir depletion will result in uniform vertical compression. The combined vertical total stress Σ_{yy} will remain equal to the initial vertical total stress σ_{yy}^0 because the weight of the overburden remains the same (no arching occurs for an infinitely wide reservoir). The incremental vertical total stress σ_{yy} will therefore be zero and the incremental pressure will result in an incremental effective vertical stress with magnitude $\sigma'_{yy} = \alpha p$. The uniaxial vertical stiffness is given by the uniaxial compaction modulus (Wang 2000, Eq. 6.5)

$$K_\nu = 2G\frac{1-\nu}{1-2\nu} = 15.79e9 \text{ Pa}, \tag{13}$$

such that with a depletion of $-25e6$ Pa, we expect a reservoir compaction, i.e. a negative change Δh of the reservoir height h (where $h = a + b$; see Fig. 1), according to

$$\Delta h = h\epsilon_{yy} = h\frac{\sigma'_{yy}}{K_\nu} = h\frac{\alpha p}{K_\nu} = -0.32 \text{ m}. \tag{14}$$

The incremental horizontal strain ϵ_{xx} remains equal to zero, because of the infinite horizontal extent of the

Fig. 3 Initial normal stresses (left) and initial shear stresses (right) along a line through the center of the reservoir at an angle of 70 deg. with horizontal

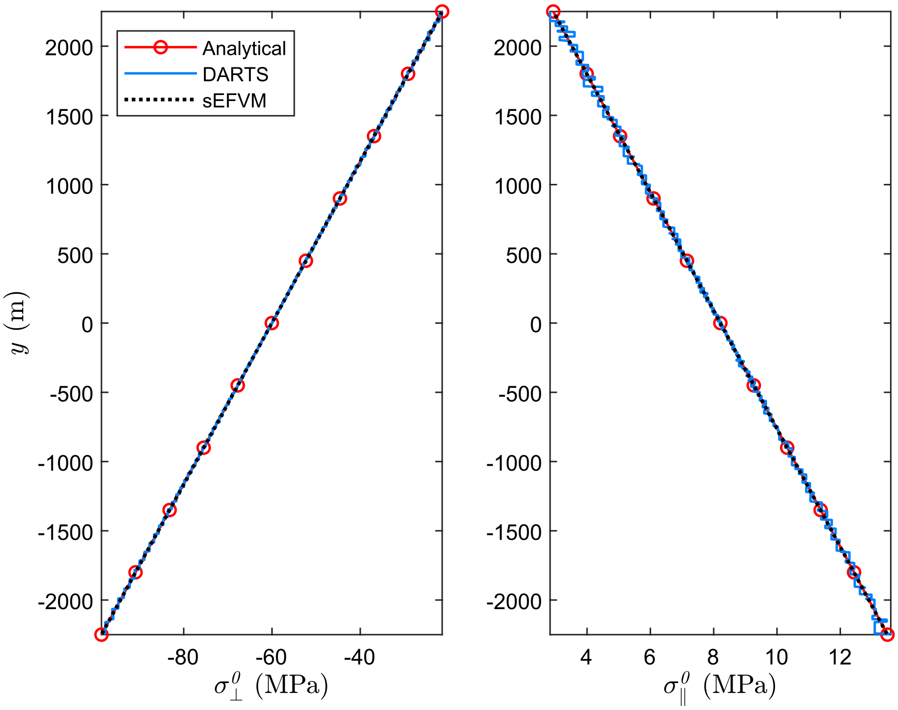

reservoir, while the incremental horizontal effective stress is equal to (Wang 2000, Eq. 6.4)

$$\sigma'_{xx} = \frac{\nu}{1-\nu}\sigma'_{yy} = \frac{\nu}{1-\nu}\alpha p = -3.97e6 \text{ Pa}, \tag{15}$$

such that the incremental total horizontal stress becomes

$$\sigma_{xx} = \sigma'_{xx} - \alpha p = 18.53e6 \text{ Pa}. \tag{16}$$

For this simple case of a reservoir without faults no incremental shear stresses σ_{xy} develop, and because there were no initial shear stresses σ_{xy}^0 it follows that also the combined shear stresses Σ_{xy} vanish. However, for the line at an angle $\theta = 70$ deg. that was considered earlier in Fig. 3, the incremental horizontal stresses σ_{xx} have an effect on both the incremental normal and shear stresses $\sigma_\perp$ and $\sigma_\parallel$, and therefore also on the combined normal and shear stresses $\Sigma_\perp$ and $\Sigma_\parallel$.

Figure 4 displays the (near-)reservoir details of $\Sigma_\perp$ and $\Sigma_\parallel$ along the inclined line for the two simulation codes and the analytical solution. Both codes produce a fully satisfactory match. We note that DARTS demonstrates a somewhat higher relative accuracy for normal stresses than for shear, especially in Fig. 3, a feature that is explained by the higher magnitude of the normal stress.

3 Depletion in a reservoir with a vertical fault with offset and no friction

Consider the same reservoir as before while introducing a displaced vertical fault at the center of the reservoir by choosing $a = 75$ m and $b = 150$ m such that the reservoir has the same height $h = a + b = 225$ m as before but now contains a fault with an offset (also known as fault throw) $t_f = b - a = 75$ m, see Fig. 5. As a first step, we don't allow for fault slip in the simulation and perform the same steps as in the previous example to generate the initial and incremental stress fields.

The combined pre-slip Coulomb stress Σ_C, i.e. the pre-slip Coulomb stress resulting from the sum of initial and incremental stresses is defined for an arbitrarily oriented fault with friction coefficient μ as

$$\Sigma_C = |\Sigma_\parallel| + \mu\Sigma_\perp. \tag{17}$$

For the particular case of a positive shear stress in a vertical fault without friction, i.e. with $\theta = 90$ degrees

Fig. 4 Combined normal stresses (left) and combined shear stresses (right) along a line through the center of the reservoir at an angle of 70 deg. with horizontal

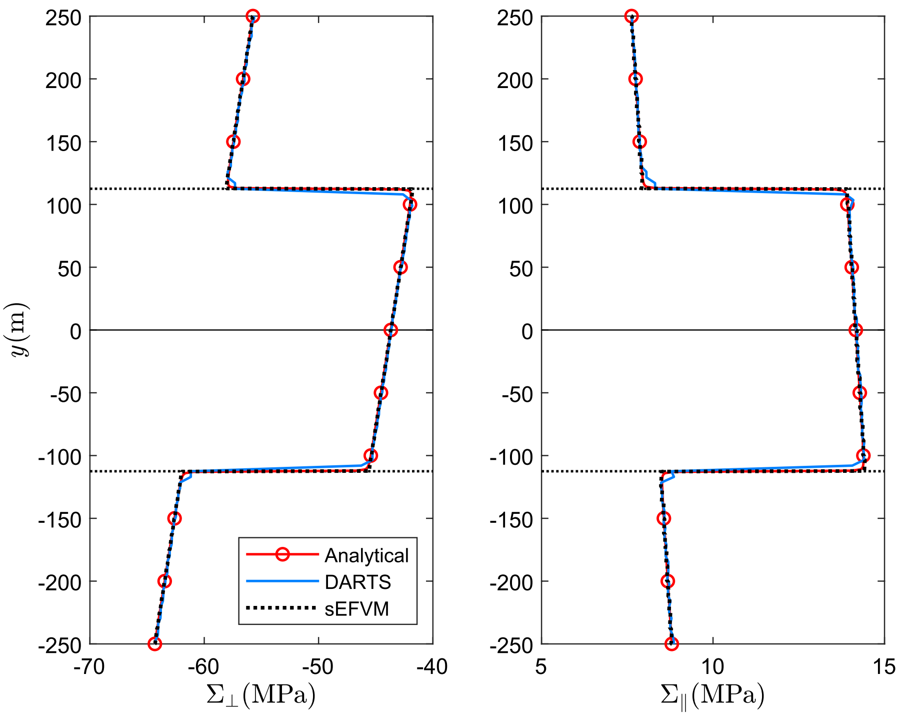

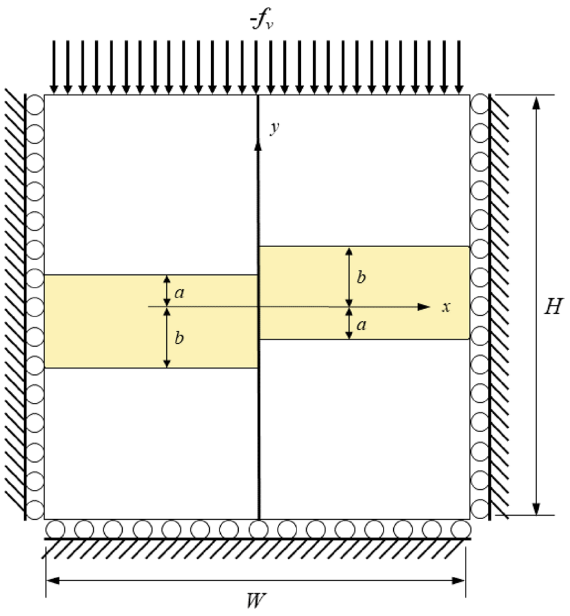

Fig. 5 Simulation set-up for a reservoir with a vertical displaced fault (not to scale)

and $\mu = 0$, and an incremental pressure of $p = -25$ MPa this reduces to (Jansen and Meulenbroek 2022, Eqs. 8 and 9)

$$\Sigma_C = -\sigma_{\hat{x}\hat{y}} = \sigma_{xy} = \frac{C}{2} \ln \frac{(y-a)^2(y+a)^2}{(y-b)^2(y+b)^2}, \tag{18}$$

where C is given by

$$C = \frac{(1-2\nu)\alpha p}{2\pi(1-\nu)} = -2.95e6\,\mathrm{Pa}. \tag{19}$$

Next, we allow for slip in the fault over the entire simulation domain, i.e. from −2250 to 2250 m. The pressure in the fault is equal to the initial pressure $p^0(y)$ except for the reservoir section $-150\,\mathrm{m} \geq y \geq 150\,\mathrm{m}$ where it is equal to the combined pressure $P = p^0(y) - 25e6$ Pa. The analytical solution for the fault slip is given by Jansen and Meulenbroek (2022, Eqs. (25) and (35))

$$\delta(y) = \frac{C}{A} \times \begin{cases} 0 & \text{if } y \leq -b, \\ -(y+b) & \text{if } -b < y \leq -a, \\ (a-b) & \text{if } -a < y < a, \\ (y-b) & \text{if } a \leq y < b, \\ 0 & \text{if } b \leq y, \end{cases} \tag{20}$$

where

Fig. 6 Left: pre-slip Coulomb stresses Σ_C in a frictionless vertical fault with offset (which, for this particular case, just equals the incremental shear stress $\sigma_{\parallel}$). Right: the resulting slip δ

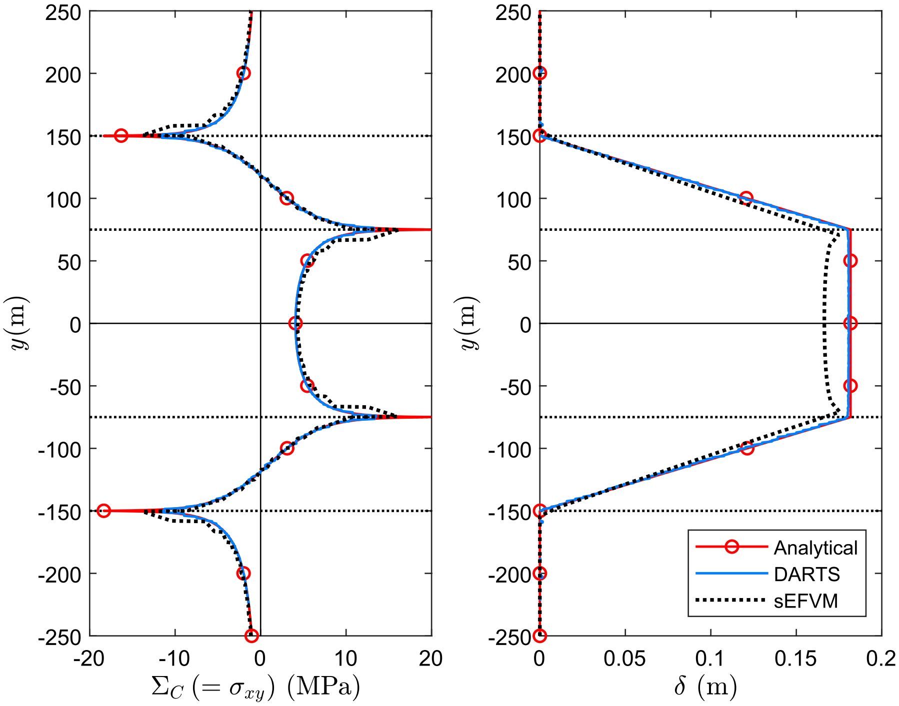

$$A = \frac{G}{2\pi(1-\nu)} = 1.2171e09\,\text{Pa}, \tag{21}$$

such that we obtain

$$\delta(y) = -0.0024 \times \begin{cases} 0 & \text{if } y \leq -150, \\ -(y+150) & \text{if } -150 < y \leq -75, \\ \quad (75-150) & \text{if } -75 < y < 75, \\ \quad (y-150) & \text{if } 75 \leq y < 150, \\ 0 & \text{if } 150 \leq y, \end{cases} \tag{22}$$

with all distances expressed in meters. Figure 6 (right) displays this slip distribution over the height of the reservoir, and Fig. 6 (left) displays the pre-slip Coulomb stress.

The correspondence between the DARTS results and the semi-analytical results is excellent. The sEFVM results are slightly in error. This is because the sEFVM calculates the slip by enriching the displacement field with one additional degree of freedom per matrix grid node. This is as opposed to other embedded methods such as XFEM, where in 2D each node that is enriched with the jump function is given two degrees of freedom. For fault tip enrichment, there are four extra degrees of freedom. This means the sEFVM is much faster in terms of CPU time, but the predictions are usually less accurate (Li et al. 2020; Xu et al. 2021).

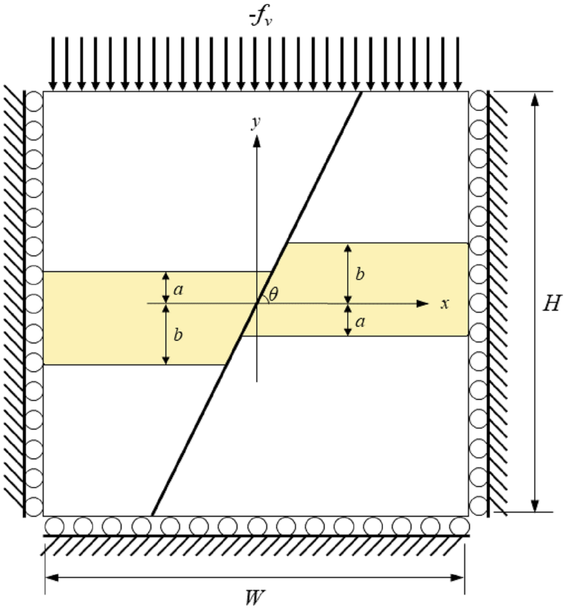

Fig. 7 Simulation set-up for a reservoir with an inclined displaced fault (not to scale)

Fig. 8 Left: pre-slip shear stresses $\Sigma_{\|}$ and slip threshold Σ_{sl} in an inclined fault with offset and constant friction. Right: the corresponding pre-slip Coulomb stresses Σ_C. Simulation domain width $W = 4500$ m

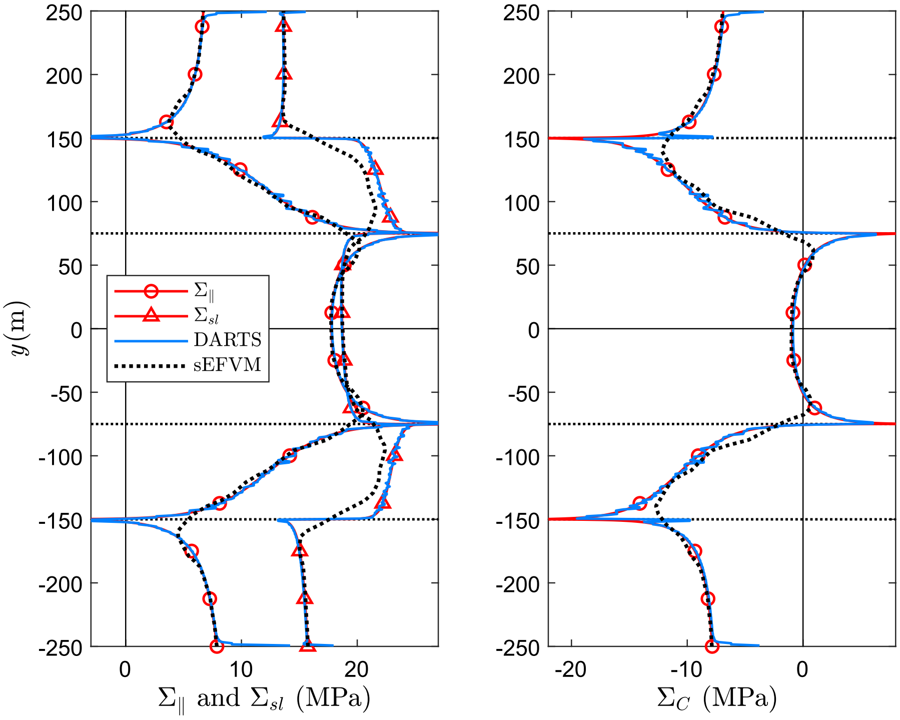

4 Depletion in a reservoir with an inclined fault with offset and friction

4.1 Constant friction

Consider the same reservoir as in the previous step but now with a normal fault at 70 deg. with respect to horizontal; see Fig. 7.

Figure 8 (left) displays the pre-slip shear stresses $\Sigma_{\|}$ and the slip threshold $\Sigma_{sl} = -\mu\Sigma'_{\perp}$ for an incremental pressure $p = -25$ MPa, and Fig. 8 (right) shows the corresponding pre-slip Coulomb stresses.

Again, the DARTS results closely resemble the semi-analytical ones, while the sEFVM results display small deviations, especially near the stress peaks at $y = \pm 75$ m and $y = \pm 150$ m. As shown in Fig. 15, the sEFVM uses a Cartesian grid with embedded faults to model the system. As a consequence, oscillations in the stress profiles can arise when the fault is misaligned with the grid. A smoothing step in the sEFVM addresses these oscillations for improved estimation of slip. However, this smoothing also flattens the peaks at $y = \pm 75$ m and $y = \pm 150$ m.

Figure 9 displays the post-slip Coulomb stresses (left) and fault slip (right) for $p = -25$ MPa. At this depletion level, the slip occurs in the form of two separate slip patches. For increasing depletion, the patches will merge as shown in the same figure with results for $p = -27$ MPa. Somewhat surprisingly the DARTS results now show a discrepancy with the semi-analytical ones, especially for the merged slip patch. Further comparisons revealed that this discrepancy disappears if the width W of the simulation domain is increased. Figure 10 displays the same results but now for a simulation with $W = 18{,}000$ m, i.e. four times as wide as the original simulation domain. Apparently, the strongly nonlinear mechanics involved in fault slip leads to strong sensitivities of the slip patch size to the boundary conditions at the edges of the reservoir. This finding suggests that in reality there will also be a large sensitivity to the boundary conditions of the reservoir and probably also a significant interaction effect of neighboring faults. Figure 11 displays the reservoir and the simulation domain, with increased width, to scale.

Figure 12 displays the location of the four slip patch boundaries (two for each of the two patches) as a function of incremental pressure. Merging occurs when the pressure has dropped to $p = -26.9$ MPa and the DARTS results (computed with $W = 18{,}000$ m) match the semi-analytical ones. The sFEVM results for Figs. 9, 10, 11 and 12 did not fully converge for

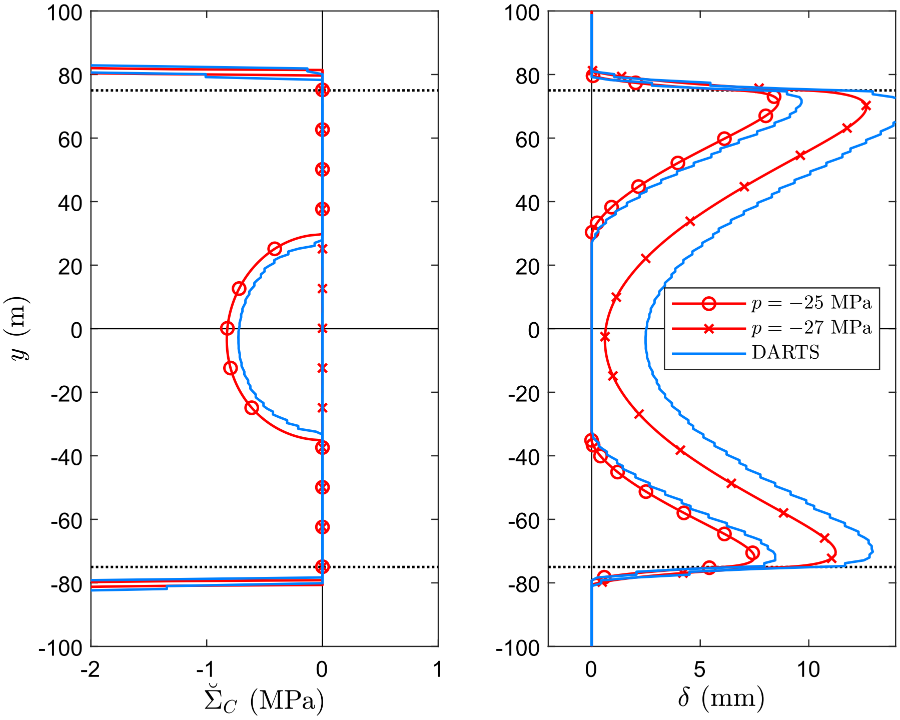

Fig. 9 Left: post-slip Coulomb stresses $\breve{\Sigma}_C$. Right: the corresponding slip δ. Simulation domain width $W = 4500$ m

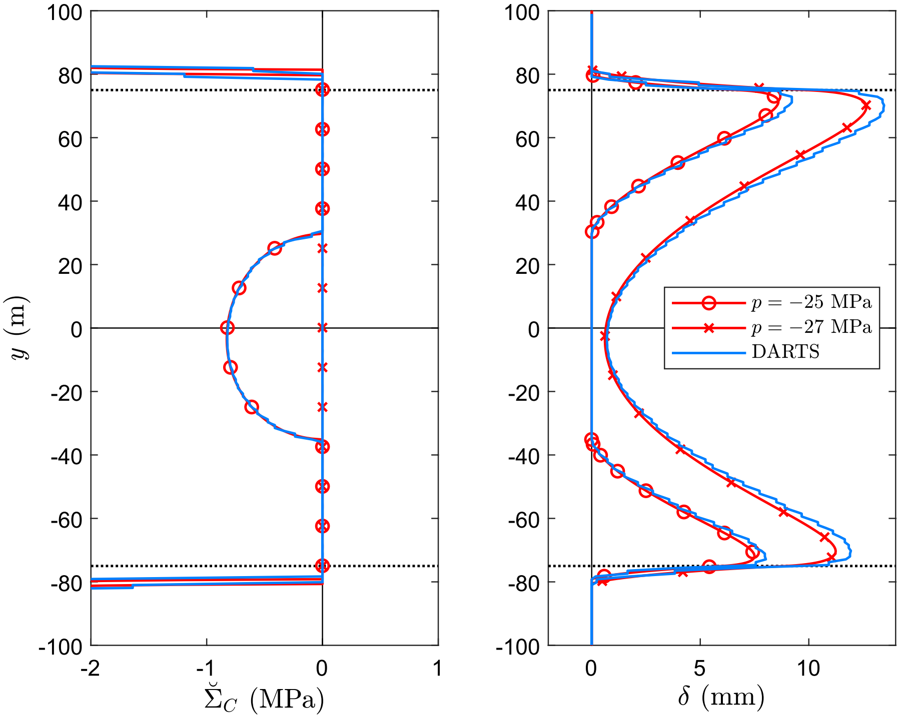

Fig. 10 Left: post-slip Coulomb stresses $\breve{\Sigma}_C$. Right: the corresponding slip δ. Simulation domain width $W = 18{,}000$ m

these test cases and displayed significant deviations from the semi-analytical results. We conclude that the characteristics of our embedded fault implementation, as were discussed at the end of in Sect. 3, hamper an accurate simulation of induced slip in this displaced fault configuration with friction.

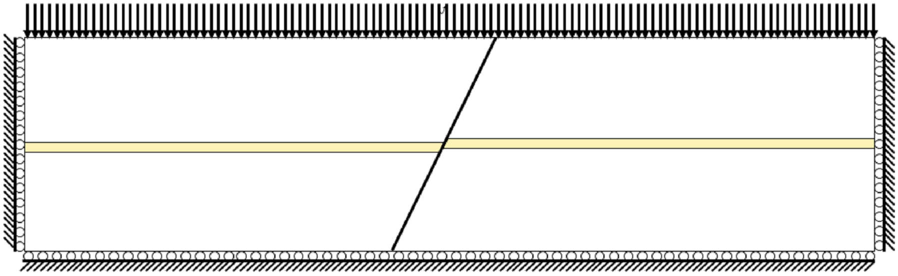

Fig. 11 Simulation set-up, with increased width $W = 18{,}000$ m, to scale

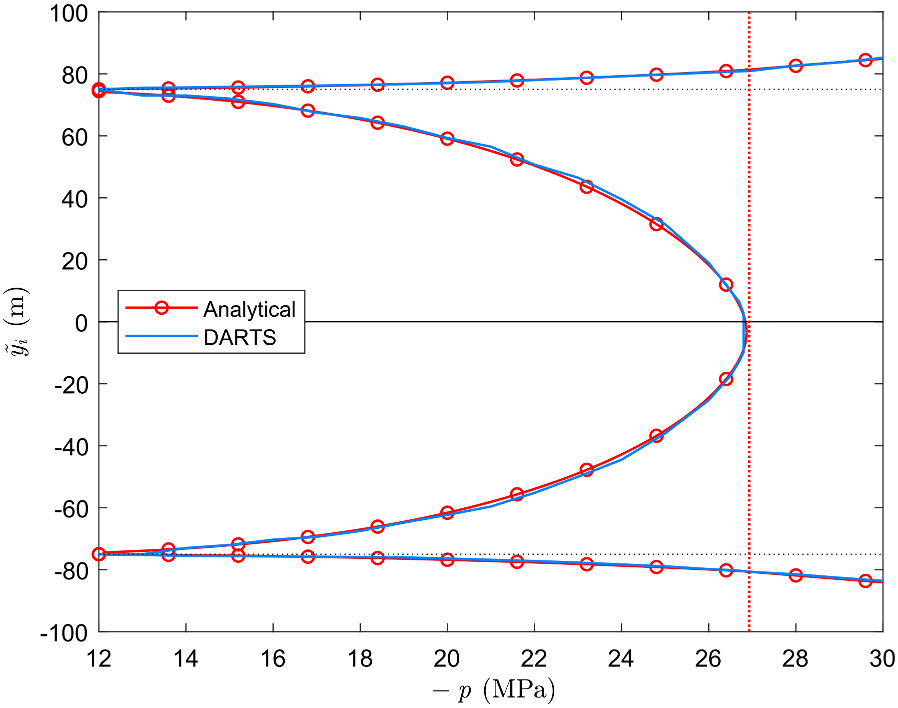

Fig. 12 Slip patch boundaries as a function of depletion pressure p. The vertical dotted line indicates the merging pressure. Simulation domain width $W = 18{,}000$ m

4.2 Slip-weakening friction

In the case of slip-weakening, friction decreases as slip increases in absolute value. We use a linear slip-weakening friction law which implies a linear decrease of the friction coefficient from a static value μ_s to a dynamic one μ_d over a critical slip distance δ_c:

$$\mu(y) = \begin{cases} \mu_{st} - (\mu_{st} - \mu_{dyn})\dfrac{|\delta(y)|}{\delta_c} & \text{if } |\delta(y)| \le \delta_c \\ \mu_{dyn} & \text{if } |\delta(y)| > \delta_c \end{cases}. \tag{23}$$

Note that the friction value remains equal to μ_d for absolute values of slip larger than δ_c, as shown in Fig. 13 for positive values of δ.

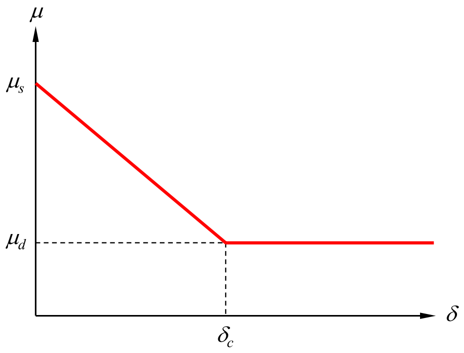

Fig. 13 Slip-weakening friction law illustrated for positive values of δ

An increase in fault slip will result in a reduction in 'carrying capacity' of the fault, and may lead to nucleation of a seismic event once a fault slip pattern has been reached in which equilibrium of shear forces is no longer possible. The corresponding depletion pressure is known as the nucleation pressure p^* (Uenishi and Rice 2003). We note that more complex friction models are required to accurately model seismic slip, such as velocity-weakening or 'rate and state' models. However slip-weakening friction is often used as a representative, albeit simple, model to describe aseismic fault slip prior to the onset of seismicity in geological formations (Ohnaka 2013). A semi-analytical approach to determine p^*, using an eigenvalue/eigenvector computation, was presented by Uenishi and Rice (2003) for a situation with a peaked shear stress and a constant normal stress along the fault. A slightly modified approach, to cope with a non-constant normal stress as in the current example, was presented by Jansen and Meulenbroek (2022).

Figure 14 illustrates the comparison of semi-analytical and numerical results for the post-slip Coulomb stresses and the slip pattern in the upper slip patch for values of the depletion pressure p just before reaching the nucleation pressure p^*. For (negative) values of p below p^*, equilibrium can no longer be computed in a quasi-static simulation, which implies that a seismic event will occur. As an aside, we note that 'run-away' rupture propagation is expected because the dynamic shear capacity utilization for $\mu_{dyn} = 0.20$ is above unity for the current fault configuration (Jansen et al. 2019). With parameter values $\mu_s = 0.52, \mu_d = 0.20$ and $\delta_c = 0.02\,\text{m}$, the semi-analytical approach predicts $p^* = -17.41\,\text{MPa}$ while DARTS arrives at $p^* = -17.27\,\text{MPa}$. The small differences in slip profiles and nucleation pressures can be explained by discretization errors inherent in numerical approximation and the effects of a finite domain width discussed in Sect. 4.1.

5 Conclusions

The study reported in this paper involved benchmarking of two recently-developed numerical methods for the simulation of induced fault slip in poroelastic reservoirs against recently-developed semi-analytical results, using test cases of increasing complexity. These concerned an unfaulted reservoir, a reservoir with a vertical frictionless displaced fault (i.e. a fault

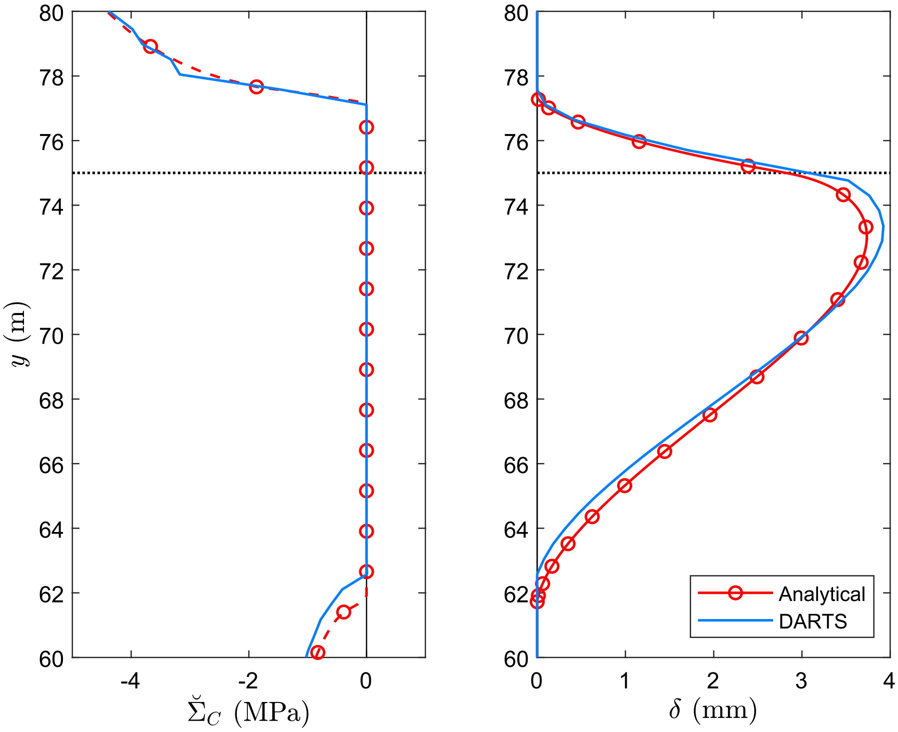

Fig. 14 Semi-analytical results (red) and numerical results (blue) for slip-weakening friction. Post-slip Coulomb stress (left) and fault slip (right) for the upper slip patch at a depletion pressure just before reaching the nucleation pressure p^*. A slip-weakening friction law is used with $\mu_s = 0.52, \mu_d = 0.20, \delta_c = 0.02\,\text{m}$ The analytical estimate for the nucleation pressure is $p^* = -17.41\,\text{MPa}$, the numerical one is $p^* = -17.27\,\text{MPa}$

with non-zero offset), and reservoirs with inclined displaced faults governed by static and slip-weakening friction laws.

Both numerical simulators are based on the finite volume (FV) method. The first one (DARTS) uses a FV collocated scheme with unstructured grids and conformal mesh, and applies a discrete fracture model (DFM). It provided a good match to the semi-analytical solutions for all test cases, including the one with a slip-weakening friction law. The second one, the smoothed embedded FV method (sEFVM), applies an embedded discrete fault model. It was found to be reasonably accurate for test cases without a fault and with a frictionless vertical displaced fault. However, for the case with an inclined displaced fault with constant friction, the sEFVM provided accurate results only for pre-slip state while it did not converge for the post-slip phase. Also, for the pre-slip state of the inclined fault, the sEFVM results were slightly less accurate than those obtained by DARTS.

The sEFVM applies Cartesian structured grids on the faulted system, with independent grids for faults and rock matrix. The current version of the method applies a FV discretization scheme which is enriched by only one degree-of-freedom per fault element. While this features makes it computationally attractive for field-scale applications, it appears to hamper accurate simulation of the slip behavior of displaced faults. Future research needs to be done to either enhance the enrichment functions within the sEFVM, or to include more enrichment points, in order to successfully capture the contact behavior of displaced faults.

In conclusion, the DFM is found to be the method of choice when accurate simulation of displaced faults is required. Its use as local solver for a global sEFVM is a possible direction for future investigations.

Author contributions AN and SSB conducted the work and developed the first draft of the manuscript. DV, HH and J-DJ supervised the work and edited the manuscript.

Funding This publication is part of the project*Science4Steer: a scientific basis for production and reinjection strategies to minimize induced seismicity in Dutch gas fields(with Project No. DEEP.NL.2018.046) of the research programme 'DeepNL' which is financed by the Dutch Research Council (NWO).*

Availibility of data and materials The semi-analytical benchmark data used to generate the figures in this paper are available in the form of an Excel file uploaded to the 4TU Data Repository: https://doi.org/10.4121/d77f1a2c-29ea-4572-ad72-e33ed8dc8d22.

Declarations

Competing interests The authors declare no potential competing interests.

Appendix 1: Collocated FVM with DFM

In this appendix we briefly describe the collocated finite volume method (FVM) with a discrete fracture model (DFM). For a more detailed description; see Novikov et al. (2022b). The system of single-phase fluid mass balance and static momentum balance equations for porous media can be written as

$$-\nabla \cdot \Sigma = (\phi \rho_f + (1-\phi)\rho_s) g \nabla y, \tag{24}$$

$$\frac{\partial}{\partial t}\left(\phi \rho_f\right) - \nabla \cdot \left(\frac{\rho_f K}{\mu_f} \left(\nabla p - \rho_f g \nabla y \right) \right) = r, \tag{25}$$

subjected to the constitutive relations (Coussy 2004)

$$\Sigma = \boldsymbol{C} : \nabla^s \left(u - u_0 \right) - pB, \tag{26}$$

$$\phi = \phi_0 + \frac{\mathrm{tr}(B) / 3 - \phi_0}{K_r}(p - p_0) + B : \nabla^s u, \tag{27}$$

where Σ is a rank-two total stress tensor, ϕ is porosity, ρ_{fl}, ρ_s are fluid and matrix densities, p is pore pressure, g is accelleration of gravity, y is depth, K is a rank-two permeability tensor, μ_f is fluid viscosity, r is a source of mass, $\boldsymbol{C}$ is a rank-four drained stiffness tensor for the rock matrix, ∇^s is the symmetric gradient operator, u is a vector of displacements, B is a rank-two tensor of Biot coefficients, subscript "0" denotes the initial value of a variable, $\mathrm{tr}(B)$ is the trace of B, and K_r is the bulk modulus of the solid phase. Equations (24), (25) are subject to corresponding boundary and initial conditions.

At the fault interfaces, we consider a gap vector g that is equal to the jump of displacements over the contact $g = u^+ - u^-$, where the + and − signs denote a particular side of the fault. The contact conditions following Simo and Laursen (1992) read

$$g_N \leq 0, \tag{28}$$

$$f'_T - \mu f'_N \frac{\dot{g}_T}{|\dot{g}_T|} = 0, \quad \Phi = 0, \quad |\dot{g}_T| \neq 0, \quad \text{(slip)}, \tag{29}$$

$$\dot{g}_T = 0, \quad \Phi < 0, \quad \text{(stick)}, \tag{30}$$

where $f = -\Sigma \cdot n$ is the total traction vector, $f' = -(\Sigma + pB) \cdot n$ is the effective (Biot) traction vector, $f'_N = n^T f'$ and $f'_T = (I - nn^T) f'$ are the scalar normal and vectorial tangential projections of f' on the fault; g_N and g_T are the equivalent normal and tangential projections of g on the fault; $\dot{g}$ stands for the time derivative of the gap vector and $\Phi = |f'_T| - \mu f'_N$ is the Coulomb friction function with μ the friction coefficient. Equation (28) represents a non-penetration condition, Eq. (29) governs relaxation of tangential traction once slip occurs, and Eq. (30) sets the change of the tangential gap (i.e. the slip) to zero if the slip criterion is not exceeded.

In the case of a collocated arrangement of unknown displacements and pore pressure, we can formulate discrete balance equations in a unified way. We use the cell-centered Finite Volume Method (FVM) to discretize Eqs. (24) and (25) (Novikov et al. 2022b, a). They can be written in cell i in the following vector form

$$V_i \begin{pmatrix} \Delta t \rho_{t,i}^{n+1} g \nabla y \\ \left(\tilde{\phi}\rho_f\right)\Big|_{i,n}^{i,n+1} + \Delta t r_i^{n+1} \end{pmatrix} + \sum_{j \in \partial V_i} \delta_{ij} \begin{pmatrix} \Delta t f_{ij}^{n+1} \\ \rho_{f\,i} \tilde{q}_{f,ij}\Big|_n^{n+1} + \Delta t (\rho_f q_f / \mu_f)_{ij}^{n+1} \end{pmatrix} = 0, \tag{31}$$

where subscript j denotes the neighbors of cell i, Δt is the time step size, V_i is the volume of cell i, δ_{ij} denotes the area of the connection between cells i and j, superscripts n, and $n+1$ denote the variables taken from the current and next time step, respectively, while $\tilde{\phi}$ and $\tilde{q}_{ij}$ are defined as

$$\tilde{\phi} = \phi_0 + \frac{\mathrm{tr}(B)/3 - \phi_0}{K_s}(p - p_0), \tag{32}$$

$$\tilde{q}_{f,ij} = \left(u - u_0\right)\Big|_i^{ij} \cdot (Bn)_{ij}, \tag{33}$$

where the last term is approximated using Gauss' formula as a sum of fluxes $\tilde{q}_{f,ij}$ over cell interfaces. The term $\left(\rho_f/\mu_f\right)_{ij}$ is calculated using an upwind approximation.

We use a gradient-based coupled multi-point stress and multi-point flux approximation for f_{ij}, $q_{f,ij}$ and $\tilde{q}_{f,ij}$ (Novikov et al. 2022b, a).

To satisfy Eqs. (28)–(30), we use a penalty regularization (Simo and Laursen 1992; Yastrebov 2013) which leads to a return-mapping algorithm according to

$$f_N'^{n+1} - \varepsilon_N \langle g_N^{n+1} \rangle = 0, \tag{34}$$

$$\widetilde{f}'_T = f_T'^{n} + \varepsilon_T (g_T^{n+1} - g_T^n), \quad \widetilde{\Phi} = \left|\widetilde{f}'_T\right| - \mu^{n+1} f_N'^{n+1}, \tag{35}$$

$$f_T'^{n+1} - \widetilde{f}'_T + \langle \widetilde{\Phi} \rangle \frac{\widetilde{f}'_T}{\left|\widetilde{f}'_T\right|} = 0, \tag{36}$$

where $\widetilde{f}'_T$ denotes a trial traction, which represents the penalized effective tangential traction (Simo and Laursen 1992). Penalty parameters $\varepsilon_N, \varepsilon_T \gg 1$ are calculated as $\varepsilon_N = f_{scale} E\delta/V$, $\varepsilon_T = f_{scale} G\delta/V$ where f_{scale} is an empirical scaling factor, δ denotes the area of the contact interface, V stands for the mean volume of two neighboring matrix cells, while E and G denote the mean Young's and shear moduli of two neighboring matrix cells (Cardiff et al. 2017). Moreover, the Coulomb friction function Φ used as a slipping criterion is evaluated at the trial state $\widetilde{\Phi} = \Phi(\widetilde{f'})$ that accounts for the change of slip g_T over the time step. Macaulay brackets are used to indicate that $\langle a \rangle$ is equal to a if $a \geq 0$ and otherwise equal to zero. Thus, in the slip state $\widetilde{\Phi} = 0$, Eq. (36) requires contact to remain at the slipping surface defined by $\Phi = 0$ where the direction of forces is defined by the trial traction. Contact reaches the stick state once the slip increment in Eq. (35) becomes negligible compared to the previous traction ($\dot{g}_T = \mathbf{0}$). In this case, Eq. (36) claims the traction to be equal to the trial one. In our experience, the return-mapping algorithm described in Eqs. (35)–(36) does not exhibit significant convergence problems, except for cases with severe inf-sup instability (pressure oscillations) and when the slip direction reverses. We may also expect convergence issues in the presence of intersecting faults or in the case of a hydraulically active fault when its volume and transmissibilities depend on the aperture g_N.

Note that we treat displacements over the lower-dimensional fault interface as discontinuous whereas pressure remains continuous there according to the assumptions of the equidimensional DFM approach. Sometimes this combination is called the mixed-dimensional fault model (Boon and Nordbotten 2022).

Appendix 2: Smoothed enhanced finite volume method

The smooth enhanced finite volume method (sEFVM) (Shokrollahzadeh Behbahani et al. 2022) uses the finite volume method (FVM) for both mechanics and flow. The mass conservation equations for a single phase, slightly-compressible flow inside a poroelastic domain with conductive faults using the embedded discrete fracture modeling (EDFM) method read (Hajibeygi et al. 2011; Li and Lee 2008),

$$\alpha\frac{\partial \nabla\cdot\vec{u}}{\partial t}+\frac{1}{M}\frac{\partial p_m}{\partial t}+\nabla\cdot\left(-\frac{K_f}{\mu_f}\cdot\nabla p_m\right)+\Psi_{m\to f}=Q_m, \tag{37}$$

and

$$\frac{\partial E_f}{\partial t}+\nabla\cdot\left(-\frac{aK_f}{\mu_f}\cdot\nabla p_f\right)+\Psi_{f\to m}=Q_f, \tag{38}$$

where p is pressure, t is time, M is the Biot modulus, Ψ is the net flux between the fault and matrix and a is aperture of the fault. E^f is the fault accumulation which is negligible if fault porosity is constant (McClure and Horne 2011). Subscripts f and m indicate the fault and matrix, respectively.

The linear momentum balance for a faulted poroelastic medium can be expressed as

$$\nabla\cdot(\tilde{\sigma}-\alpha p\tilde{I})+\vec{f}=0, \tag{39}$$

where $\tilde{\sigma}$ is the effective stress, $\vec{f}$ is the body force per unit volume and $\tilde{I}$ is the identity matrix (Wang 2000, Eq. 4.10). Assuming linear elastic deformation, the stress reads

$$\tilde{\sigma}=\tilde{C}:\nabla^{s}\vec{u}, \tag{40}$$

where $\tilde{C}$ is the elasticity tensor (Wang 2000, Eq. 2.42).

The sEFVM determines a nonzero value for the fault slip whenever the Coulomb stresses on a fault node become positive. Further details on the governing equations and initial and boundary conditions are described in Shokrollahzadeh Behbahani et al. (2022).

The computational domain of the sEFVM is shown in Fig. 15. It shows the control volumes for mechanics (Ω_u) and flow (Ω_p) for the matrix. Faults are represented in an embedded manner with unknowns (slip and fault pressure) placed at the location of the fault.

In the sEFVM, a jump is appended to the estimation of the displacement field inside a matrix grid (Simo et al. 1993). The displacement reads

$$\vec{u}\approx\sum_{i=1}^{4}N_i\vec{u}_i+\sum_{i=1}^{n_s}s_iW_i\vec{t}_i, \tag{41}$$

where N are basis functions that interpolate displacement within the cartesian control volume of Fig. 15. For cells intersected by faults, the latter term in Eq. (41) is included. It contains the directional component of the unit tangent vector to the fault ($\vec{t}$). W is defined as

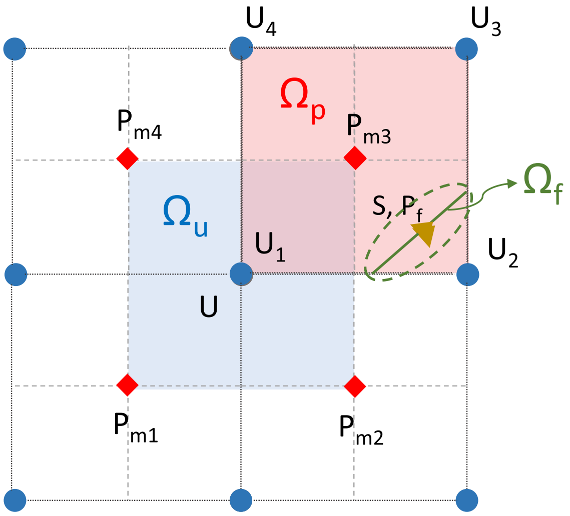

Fig. 15 Representation of the control volumes for the sEFMV method

$$W(x,y) = \sum_{i=1}^{4} N_i(x,y) \left[H\Big(f(x,y)\Big) - H\Big(f\left(x_i, y_i\right)\Big) \right], \tag{42}$$

where $f(x, y)$ is the signed distance to the fault and H is a modified Heaviside function defined as

$$H(\zeta) = \begin{cases} -1 & \zeta \leq 0 \\ +1 & \zeta > 0 \end{cases}. \tag{43}$$

The sEFVM numerically solves the momentum balance for the matrix, the friction law for the faults, and the mass balance equations for matrix and faults in a fully-implicit fully-coupled manner.

Appendix 3: Grids used in calculations

The DFM concept implies a computational grid to be conformal with faults. We use unstructured triangular grids shown in the left column in Fig. 16. Grid refinement helps to resolve discontinuities along the fault. Characteristic grid sizes used in calculations are listed in Table. 3. The sEFVM uses a Cartesian grid for the matrix and the fault is embedded over it as shown in the right column in Fig. 16. All sEFVM runs were performed for a cell size of 8.3m.

Appendix 4: Semi-analytical techniques

Details of the semi-analytical techniques used to generate the results in this paper have been reported in Jansen et al. (2019), Jansen and Meulenbroek (2022), Cornelissen et al. (2024) and Meulenbroek and Jansen (2024). Here we give a brief overview of these methods.

4.1 Inclusion theory

Linear elastic displacements, strains and stresses inside and outside a reservoir undergoing injection or production can be determined with the 'theory of inclusions' as introduced by Eshelby (1957). Identical expressions can be obtained from potential theory and the related 'nucleus of strain concept' (Goodier 1937; Timoshenko and Goodier 1970; Geertsma 1973; Rudnicki 2002; Lehner et al. 2005). Inclusion theory and the nucleus of strain concept have been applied to compute subsidence (Geertsma 1966, 1973), and stress fields around producing reservoirs to establish the risk on reactivation of nearby (nondisplaced) faults (Segall 1985, 1989; Segall and Fitzgerald 1998; Soltanzadeh and Hawkes 2008). For in-depth derivations, see Mura (1987) and Rudnicki (2011).

The remainder of this subsection is largely identical to the description in Cornelissen et al. (2024) which, in turn is based on the Supplementary Information belonging to Jansen et al. (2019). Consider a homogeneous porous and permeable inclusion undergoing an increase of pore pressure inside a homogeneous infinite domain with the same elastic proper- ties as the inclusion. Flow to or from the outer domain is not possible. An increase in pore pressure in the inclusion causes a reduction in effective stress in its matrix and consequently an elastic expansion of the inclusion. Figure 17 depicts a series of imaginary steps that allow for computing the displacements in and around the expanding inclusion as first described by Eshelby (1957):

1. Remove the inclusion from its surroundings.
2. Allow the inclusion to expand freely in response to a change in pore pressure.
3. Restore the inclusion to its original shape by applying distributed forces at its boundaries.
4. Re-attach the inclusion to its surroundings and remove the forces (i.e., apply the forces in opposite direction to the entire infinite solid).

If the inclusion would be allowed to expand stress-free, as in step 2 above, it would experience a uniform dilational deformation. The corresponding strain tensor is often referred to as the *transformation strain*, *stress-free strain*, or *eigenstrain*, has components (Wang 2000, p. 38)

$$\epsilon_{ij}^{*} = \frac{\alpha p}{3K} \delta_{ij} \delta_{\Omega}, \tag{44}$$

where $\alpha = 1 - c_s / c_m$ is Biot's coefficient, with c_s the compressibility of the solid phase and c_m the drained compressibility of the porous medium, K is the drained pore bulk modulus, δ_{ij} is the regular Kronecker delta, and δ_{Ω} is a modified Kronecker delta that equals 1 inside the inclusion and 0 outside. No strains would develop outside the inclusion as a result of step 2.

Fig. 16 Computational grids used in calculations. The grids in the left column (**a**, **c**, **e**) were used by the collocated FV with DFM (DARTS) while the grids from the right column were used by the sEFVM. The collocated FV with DFM (DARTS) uses adaptive triangular grids. The grid size is scaled for convenient representation, the real grid size is listed in Table 3. In the initial stage, the grid is adaptively refined towards the reservoir, in the presence of a fault—towards the fault. The sEFVM uses Cartesian grids with embedded faults. The grid size is also scaled for convenient representation

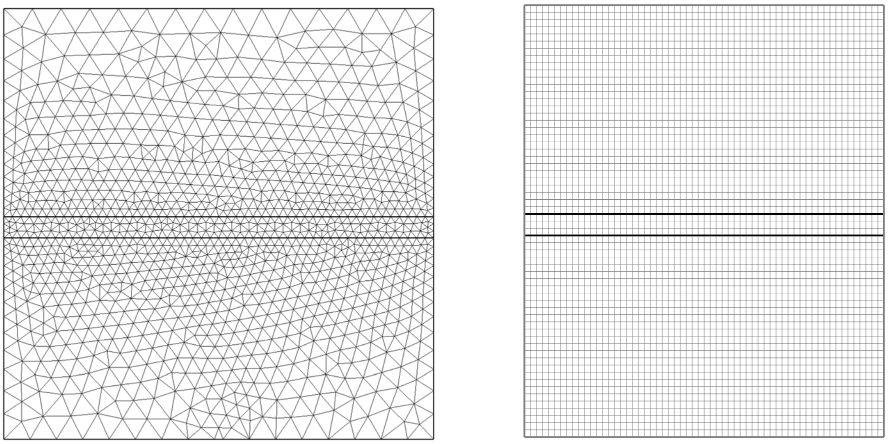

(a) No fault (DARTS) (b) No fault (sEFVM)

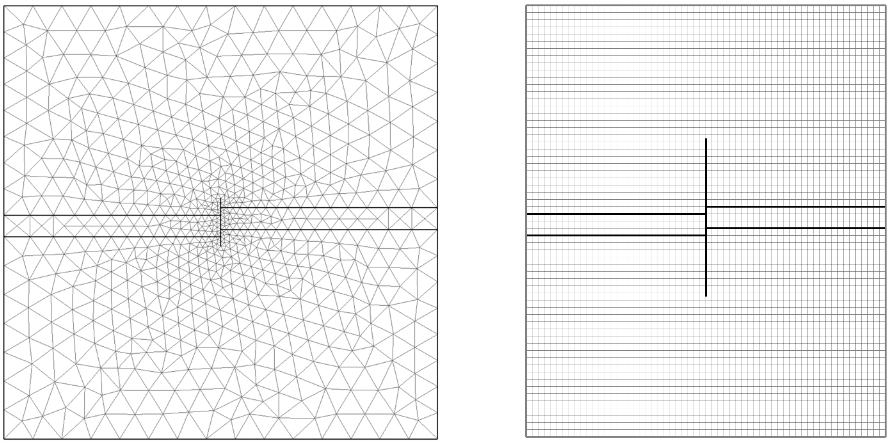

(c) Vertical fault (DARTS) (d) Vertical fault (sEFVM)

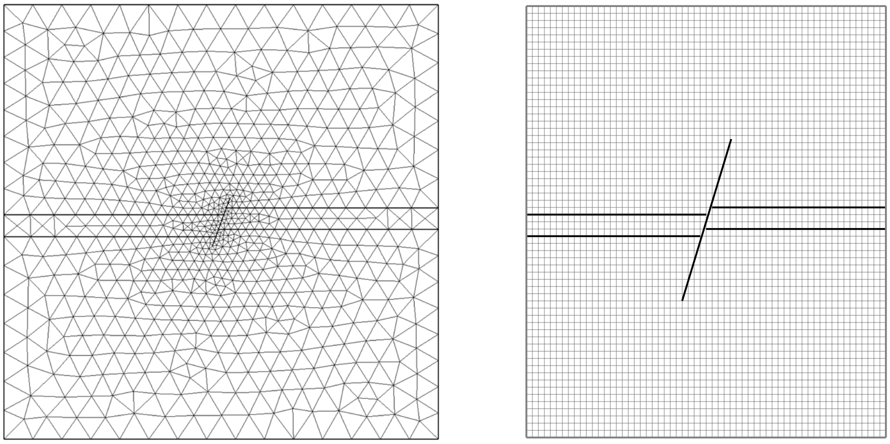

(e) Inclined fault (DARTS) (f) Inclined fault (sEFVM)

Table 3 The cell size of adaptive grids shown in the left column in Fig. 16

Case	Boundary cell size, m	Refined cell size, m
Without fault	50	20
With fault	100	2

The inclusion can be brought back to its original shape and size by applying surface tractions with magnitude $-\sigma^*_{ij} n_j$ to the boundary of the inclusion, where σ^*_{ij} is obtained from the transformation strain via Hooke's law

$$\sigma^*_{ij} = -(\lambda \delta_{ij} \epsilon^*_{kk} + 2\mu \epsilon^*_{ij}) = -\alpha p \delta_{ij} \delta_\Omega, \tag{45}$$

where λ and μ are Lamé's first and second parameter, respectively, repeated indices imply summation, and n_i denotes the i-component of the outward normal vector of the inclusion boundary. The stress tensor σ^*_{ij} is generally referred to as the *eigenstress* (not to be confused with the principal stresses, which are computed from the eigenvalues of the stress tensor). At the end of step 3, the strain equals zero everywhere, while the stress inside the inclusion equals σ^*_{ij} and vanishes outside of the inclusion.

Next, we reconnect the inclusion to the surrounding material and remove the distributed forces by applying their negatives. The resulting displacement field can be computed from

$$u_i(\mathbf{x}) = \alpha p \int_\Gamma g_{ij} n_j \, d\Gamma, \tag{46}$$

where u_i is the displacement in the i-direction and g_{ij} are Green's functions, which denote the displacement in the i-direction at point $\mathbf{x}$ due to an applied force in the j-direction at point $\mathbf{x}'$ Love (1927). Applying the divergence theorem allows us to transform the surface integral in Eq. (46) into a volume integral

$$u_i(\mathbf{x}) = \alpha p \int_\Omega g_{ij,j}(\mathbf{x}, \mathbf{x}') \, d\Omega, \tag{47}$$

where a comma is used to indicate differentiation. The displacement field described by Eq. (47) is due to a distribution of centers of dilatation (i.e., double forces without moment in all perpendicular directions), also referred to as nuclei of strain.

Once the displacement field is known from Eq. (47), the total strains ϵ_{ij} can be obtained from the compatibility equation

$$\epsilon_{ij} = \frac{1}{2}\left(u_{j,i} + u_{i,j}\right). \tag{48}$$

The stresses can be obtained from the strains by Hooke's law. However, for points inside the inclusion Ω it is necessary to add the eigenstress defined in Eq. (45) (Mura 1987). The stresses are then given by

$$\sigma_{ij} = \lambda \delta_{ij} \epsilon_{kk} + 2\mu \epsilon_{ij} - \alpha p \delta_{ij} \delta_\Omega, \tag{49}$$

which is equivalent to the poroelastic form of Hooke's law (Wang 2000).

Jansen et al. (2019) used this method to derive 2D closed-form expressions for the depletion-induced or injection-induced stresses in an inclined displaced fault, i.e. a fault with a nonzero offset. Similar expressions were published concurrently by Lehner (2019) and later by Wu et al. (2021), while further results and an analysis of some

Fig. 17 Imaginary steps involved in computing the displacements in and around an expanding inclusion in an infinite solid

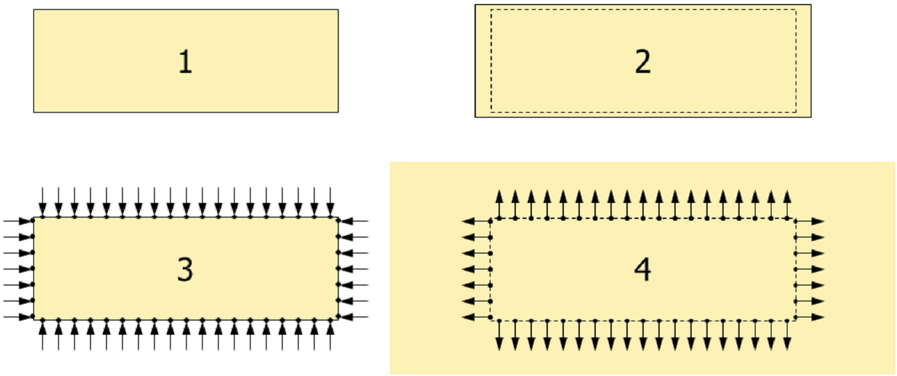

mathematical aspects were recently published by Cornelissen et al. (2024).

4.2 Cauchy integrals and Chebyshev polynomials

Inclusion theory (or, alternatively, numerical techniques) can be used to compute the injection-induced or depletion-induced pre-slip Coulomb stress in a fault, defined as

$$\Sigma_C = \Sigma_{\|} - \Sigma_{sl} = \Sigma_{\|} + \mu \Sigma'_{\perp}, \tag{50}$$

where $\Sigma_{\|}$ is the shear stress, Σ_{sl} the slip threshold, $\Sigma'_{\perp}$ the effective normal stress and μ the friction coefficient. Note that we use a sign convention where positive stresses correspond to tension.

In case of depletion, the sharp 'internal' and 'external' reservoir-fault corners in the reservoir models displayed in Figs. 5 and 7 result in positive-valued peaks in the pre-slip Coulomb stress at $y = \pm a$ and negative-valued peaks at $y = \pm b$, see Figs. 6 and 8. These peaks are, mathematically, of infinite magnitude. In reality, physical effects such as more rounded corners, a finite fault width and pore pressure diffusion between the reservoir and the surrounding rock will somewhat smoothen the stress profile. However, peaks in the pre-slip Coulomb stress profile remain a typical characteristic of displaced faults that experience depletion or injection where it should be noted that as opposed to the peak configuration during depletion, injection results in positive peaks at the external corners and negative peaks at the internal ones (Jansen et al. 2019).

In areas where the pre-slip Coulomb stress is positive, fault slip will occur. However, once slip occurs the stress field in and around the fault changes. In particular, slip-induced shear stresses in the fault occur, which can be shown to have magnitude (Bilby and Eshelby 1968)

$$\begin{aligned} \breve{\sigma}_{\|}(y) = -\Sigma_C(y) &= A \int_{-\infty}^{\infty} \frac{\nabla\delta(\xi)}{\xi - y}\, d\xi \\ &= A\left(\int_{\tilde{y}_1}^{\tilde{y}_2} \frac{\nabla\delta(\xi)}{\xi - y}\, d\xi + \int_{\tilde{y}_3}^{\tilde{y}_4} \frac{\nabla\delta(\xi)}{\xi - y}\, d\xi \right), \end{aligned} \tag{51}$$

where, for plane-strain conditions,

$$A = \frac{G}{2\pi(1-\nu)}, \tag{52}$$

with G representing the shear modulus and ν Poisson's ratio, and

$$\nabla\delta(\xi) = \left.\frac{\partial\delta(y)}{\partial y}\right|_{y=\xi}, \tag{53}$$

with δ representing the slip and $\nabla\delta(y)$ the slip gradient along the fault. The variables $\tilde{y}_i, i = 1, ..., 4$, in Eq. (51) are horizontal projections on the y axis of the lower and upper slip patch boundaries.

The integrands in Eq. (51) become singular when $\xi = y$. The integrals are therefore Cauchy-type singular integrals which implies that they have to be interpreted in a principal value sense.

For a known pre-slip Coulomb stress distribution Σ_C, both the slip gradient $\nabla\delta(y)$ and the patch boundaries $\tilde{y}_i$ are unknowns that have to be determined from the inverse of Eq. (51) and additional conditions. Muskhelishvili (1953) proved that an analytical inversion of singular integral equations can be obtained provided the known function in the integrand is Hölder continuous, which is a stricter form of continuity than regular continuity as applied in mathematical analysis. The closed-form expressions for induced pre-slip Coulomb stresses in a displaced fault contain jump discontinuities at coordinate values $y = \{-b, -a, a, b\}$ in addition to singularities in the form of infinite stress peaks. The jump discontinuities clearly violate the regular and Hölder continuity conditions. An effective way to overcome this difficulty is to regularize the expressions for the shear and normal stresses in the fault, an approach that was followed by Jansen and Meulenbroek (2022).

Cauchy integrals and their corresponding inverse expressions can often be manipulated efficiently with the aid of Chebyshev polynomials (Mason and Handscomb 2003). Applications in aerodynamics, contact mechanics and fracture mechanics involve both semi-analytical approaches, and numerical methods that strongly rely on the underlying analytical properties of Chebyshev polynomials. Semi-analytical solutions have been applied to model fault slip by Uenishi and Rice (2003); Segall (2010); Van Wees et al. (2019) and Jansen and Meulenbroek (2022).

Using these semi-analytical techniques the development of fault slip can be determined as a function of increasing injection or depletion. Fault slip, which initiates around the peaks in the pre-slip Coulomb stresses, may trigger seismicity in a critically stressed fault, but may also be aseismic, a situation corresponding to the patch growth in Fig. 12. Depending on the friction characteristics of the fault, continuing depletion may result in a gradual aseismic growth of the two slip patches possibly leading to merging. Alternatively, increasing depletion may lead to an unstable situation resulting in a seismic event, see, e.g. Van den Bogert (2015, 2018); Buijze et al. (2017, 2019) and Van Wees et al. (2017) who performed numerical studies into depletion-induced seismicity in displaced faults. A detailed semi-analytical treatment of this phenomenon was reported by Jansen and Meulenbroek (2022). At large depletion values, when the stress peaks approach each other, their mutual interaction can no longer be neglected. A detailed analysis of this coupling effect is presented in Meulenbroek and Jansen (2024).

The semi-analytical benchmark data used to generate the figures in this paper are available in the form of an Excel file uploaded to the 4TU Data Repository: https://doi.org/10.4121/d77f1a2c-29ea-4572-ad72-e33ed8dc8d22.

References

Atkinson GM, Eaton DW, Ghofrani H, Walker D, Cheadle B, Schultz R, Shcherbakov R, Tiampo K, Gu J, Harrington RM, Liu Y, Van Der Baan M, Kao H (2016) Hydraulic fracturing and seismicity in the Western Canada sedimentary basin. Seismol Res Lett 87(3):631–647. https://doi.org/10.1785/0220150263

Berge RL, Berre I, Keilegavlen E, Nordbotten JM, Wohlmuth B (2020) Finite volume discretization for poroelastic media with fractures modeled by contact mechanics. Int J Numer Methods Eng 121(4):644–663. https://doi.org/10.1002/nme.6238

Bilby BA, Eshelby JD (1968). In: Liebowitz H (ed) Dislocations and the theory of fracture, vol 1. Academic Press, New York, pp 99–182

Boon WM, Nordbotten JM (2022) Mixed-dimensional poromechanical models of fractured porous media. Acta Mechanica. https://doi.org/10.1007/s00707-022-03378-1

Buijze AJL, Van den Bogert P, Wassing B, Orlic B, Ten Veen J (2017) Fault reactivation mechanisms and dynamic rupture modelling of production-induced seismic events in a Rotliegend gas reservoir. Neth J Geosci 96:131–148. https://doi.org/10.1017/njg.2017.27

Buijze AJL, Van den Bogert P, Wassing B, Orlic B (2019) Nucleation and arrest of dynamic rupture induced by reservoir depletion. J Geophys Res Solid Earth 124:3620–3645. https://doi.org/10.1029/2018JB016941

Buijze L, Van Bijsterveldt L, Cremer H, Paap B, Veldkamp H, Wassing BBT, Van Wees J-D, Van Yperen GCN, Ter Heege JH (2020) Review of induced seismicity in geothermal systems worldwide and implications for geothermal systems in the Netherlands. Geologie en Mijnbouw/Neth J Geosci. https://doi.org/10.1017/njg.2019.6

Carder DS (1945) Seismic investigations in the Boulder Dam area, 1940–1944, and the influence of reservoir loading on local earthquake activity. Bull Seismol Soc Am 35(4):175–192. https://doi.org/10.1785/BSSA0350040175

Cornelissen P, Jansen JD (2023) Steady-state flow through a subsurface reservoir with a displaced fault and its poroelastic effects on fault stresses. Transp Porous Media. https://doi.org/10.1007/s11242-023-02029-w

Cheng Y, Liu W, Xu T, Zhang Y, Zhang X, Xing Y, Feng B, Xia Y (2023) Seismicity induced by geological CO2 storage: a review. Earth-Sci Rev. https://doi.org/10.1016/j.earscirev.2023.104369

Cornelissen P, Meulenbroek BJ, Jansen JD (2024) On the derivation of closed-form expressions for displacements, strains and stresses inside a poroelastic inclusion. J Geophys Res Solid Earth. https://doi.org/10.1029/2023JB027733

Coussy O (2004) Poromechanics, 2nd edn. Wiley, Chichester

Cardiff P, Tukovic Z, Jaeger PD, Clancy M, Ivankovic A (2017) A Lagrangian cell-centred finite volume method for metal forming simulation. Int J Numer Methods Eng 109(13):1777–1803. https://doi.org/10.1002/nme.5345

Cusini M, White JA, Castelletto N, Settgast RR (2021) Simulation of coupled multiphase flow and geomechanics in porous media with embedded discrete fractures. Int J Numer Anal Methods Geomech 45(5):563–584. https://doi.org/10.1002/nag.3168

Deb R, Jenny P (2017) Finite volume-based modeling of flow-induced shear failure along fracture manifolds. Int

J Numer Anal Methods Geomech 41(18):1922–1942. https://doi.org/10.1002/nag.2707

Davis SD, Pennington WD (1989) Induced seismic deformation in the Cogdell oil field of West Texas. Bull Seismol Soc Am 79(5):1477–1495

Elk J, Doornhof D, Bommer JJ, Bourne SJ, Oates SJ, Pinho R, Crowley H (2017) Hazard and risk assessments for induced seismicity in Groningen. Neth J Geosci 96(5):259–269. https://doi.org/10.1017/njg.2017.37

Ellsworth WL, Giardini D, Townend J, Ge S, Shimamoto T (2019) Triggering of the Pohang, Korea, earthquake (Mw 5.5) by enhanced geothermal system stimulation. Seismol Res Lett 90(5):1844–1858. https://doi.org/10.1785/0220190102

Eshelby JD (1957) The determination of the elastic field of an ellipsoidal inclusion and related problems. Proc R Soc Lond Ser A 241:376–396. https://doi.org/10.1098/rspa.1957.0133

Franceschini A, Gazzola L, Ferronato M (2022) A scalable preconditioning framework for stabilized contact mechanics with hydraulically active fractures. J Comput Phys. https://doi.org/10.1016/j.jcp.2022.111276

Geertsma J (1966) Problems of rock mechanics in petroleum production engineering. In: Proceedings of the 1st ISRM congress, 25 Sept–1 Oct, Lisbon, Portugal

Geertsma J (1973) A basic theory of subsidence due to reservoir compaction: the homogeneous case. Verhandelingen Koninklijk Nederlandsch Geologisch Mijnbowkundig Genootschap 2S:43–61

Garipov TT, Hui MH (2019) Discrete fracture modeling approach for simulating coupled thermo-hydro-mechanical effects in fractured reservoirs. Int J Rock Mech Mining Sci. https://doi.org/10.1016/j.ijrmms.2019.104075

Garipov TT, Karimi-Fard M, Tchelepi HA (2016) Discrete fracture model for coupled flow and geomechanics. Comput Geosci 20(1):149–160. https://doi.org/10.1007/s10596-015-9554-z

Goodier JN (1937) On the integration of the thermo-elastic equations. Lond Edinb Dublin Philos Mag J Sci 23:1017–1032. https://doi.org/10.1080/14786443708561872

Gupta HK (2002) A review of recent studies of triggered earthquakes by artificial water reservoirs with special emphasis on earthquakes in Koyna, India. Earth Sci Rev 58(3–4):279–310. https://doi.org/10.1016/S0012-8252(02)00063-6

Hills DA, Kelly PA, Dai DN, Korsunsky AM (1996) Solution of crack problems: the distributed dislocation technique. Kluwer Academic Publishers, Dordrecht

Hajibeygi H, Karvounis D, Jenny P (2011) A hierarchical fracture model for the iterative multiscale finite volume method. J Comput Phys 230(24):8729–8743. https://doi.org/10.1016/j.jcp.2011.08.021

Healy JH, Rubey WW, Griggs DT, Raleigh CB (1968) The Denver earthquakes. Science 161(3848):1301–1310. https://doi.org/10.1126/science.161.3848.1301

Han Z, Younis RM (2023) Adaptive time-stepping to capture induced seismicity for unconventional reservoir exploration. https://doi.org/10.15530/urtec-2023-3862235.

Jha B, Juanes R (2014) Coupled multiphase flow and poromechanics: a computational model of pore pressure effects on fault slip and earthquake triggering. Water Resour Res 50(5):3776–3808. https://doi.org/10.1002/2013WR015175

Jansen JD, Meulenbroek BJ (2022) Induced aseismic slip and the onset of seismicity in displaced faults. Neth J Geosci. https://doi.org/10.1017/njg.2022.9

Jansen JD, Singhal P, Vossepoel FC (2019) Insights from closed-form expressions for injection- and production-induced stresses in displaced faults. J Geophys Res Solid Earth 124:7193–7212. https://doi.org/10.1029/2019JB017932

Keilegavlen E, Duboeuf L, Dichiarante AM, Halldorsdottir S, Stefansson I, Naumann M, Gudnason EA, Agustsson K, Eggertsson GH, Oye V, Berre I (2021) Hydro-mechanical simulation and analysis of induced seismicity for a hydraulic stimulation test at the Reykjanes geothermal field, iceland. Geothermics. https://doi.org/10.1016/j.geothermics.2021.102223

Kim W-Y (2013) Induced seismicity associated with fluid injection into a deep well in Youngstown, Ohio. J Geophys Res Solid Earth 118(7):3506–3518. https://doi.org/10.1002/jgrb.50247

Keranen KM, Weingarten M (2018) Induced seismicity. Annu Rev Earth Planet Sci 46:149–174. https://doi.org/10.1146/annurev-earth-082517-010054

Lehner F (2019) An analysis of depletion-induced fault stressing: new closed-form analytical solutions. Technical report, Nederlandse Aardolie Maatschappij. http://www.nam.nl/feiten-en-cijfers/onderzoeksrapporten.html

Li L, Lee SH et al (2008) Efficient field-scale simulation of black oil in a naturally fractured reservoir through discrete fracture networks and homogenized media. SPE Reserv Eval Eng 11(04):750–758. https://doi.org/10.2118/103901-MS

Li T, Han D, Yang F, Yu B, Sun D, Wei J (2020) A comparative study on simulating flow-induced fracture deformation in subsurface media by means of extended FEM and FVM. Oil Gas Sci Technol Revue IFP Energies nouvelles 75:41. https://doi.org/10.2516/ogst/2020037

Lehner FK, Knoglinger JK, Fisher FD (2005) Use of a Maysel integral representation for solving poroelastic inclusion problems. In: Ziegler F, Heuer R, Adam C (eds) Proceedings of international congress on thermal stresses. TU Wien, Vienna, pp 77–80

Love AEH (1927) A treatise on the mathematical theory of elasticity, 4th edn. Cambridge University Press, Cambridge

Mavko GM (1982) Easy computation of static stress drop, slip, and moment on two-dimensional heterogeneous faults. Bull Seismol Soc Am 72:1499–1508

Muntendam-Bos AG, Hoedeman Polychronopoulou K, Draganov D, Weemstra C, Zee W, Bakker RR, Roest H (2022) An overview of induced seismicity in the Netherlands. Neth J Geosci. https://doi.org/10.1017/njg.2021.14

Majer EL, Baria R, Stark M, Oates S, Bommer J, Smith B, Asanuma H (2007) Induced seismicity associated with enhanced geothermal systems. Geothermics 36(3):185–222. https://doi.org/10.1016/j.geothermics.2007.03.003

Mason JC, Handscomb DC (2003) Chebyshev polynomials. CRC Press, Boca Raton

McClure MW, Horne RN (2011) Investigation of injection-induced seismicity using a coupled fluid flow and rate/state friction model. Geophysics 76(6):181–198. https://doi.org/10.1190/geo2011-0064.1

Meulenbroek BJ, Jansen JD (2024) The use of Cauchy-type singular integrals over neighboring intervals to compute induced slip in displaced faults. Int J Solids Struct 300:112922. https://doi.org/10.1016/j.ijsolstr.2024.112922

McGarr A, Simpson D, Seeber L (2002) 40 case histories of induced and triggered seismicity. Int Geophys 81(PART A):647–661. https://doi.org/10.1016/S0074-6142(02)80243-1

Mura T (1987) Micromechanics of defects in solids, 2nd edn. Martinus Nijhoff Publishers, Dordrecht

Muskhelishvili NI (1953) Singular integral equations. Wolters-Noordhoff, Groningen

Nordbotten JM (2014) Cell-centered finite volume discretizations for deformable porous media. Int J Numer Methods Eng 100(6):399–418. https://doi.org/10.1002/nme.4734

Novikov A, Voskov D, Hajibeygi H, Jansen JD (2022a) Collocated finite volume scheme for scalable simulation of induced seismicity. In: 18th European conference on the mathematics of oil recovery, ECMOR 2022, pp 1–18. https://doi.org/10.3997/2214-4609.202244103

Novikov A, Voskov DV, Khait M, Hajibeygi H, Jansen JD (2022b) A scalable collocated finite volume scheme for simulation of induced fault slip. J Comput Phys 469:111598. https://doi.org/10.1016/j.jcp.2022.111598

NWO: DeepNL Research Programme. https://www.nwo.nl/en/researchprogrammes/deepnl. Accessed 2022-03-31

Ohnaka M (2013) The physics of rock failure and earthquakes. Cambridge University Press, Cambridge

Riemer KL, Durrheim RJ (2012) Mining seismicity in the Witwatersrand Basin: monitoring, mechanisms and mitigation strategies in perspective. J Rock Mech Geotech Eng 4(3):228–249. https://doi.org/10.3724/SP.J.1235.2012.00228

Rudnicki JW (2002) Elsheby transformations, pore pressure and fluid mass changes, and subsidence. In: Poromechanics II, 2nd Biot Conference on Poromechanics. https://doi.org/10.1201/9781003078807-47. Aug. 26–28, Grenoble, France

Rudnicki JW (2011). In: Leroy YM, Lehner FK (eds) Eshelby's technique for analyzing inhomogeneities in geomechanics. Springer, Vienna, pp 43–72. https://doi.org/10.1007/978-3-7091-0939-7_2

Sokolova I, Bastisya MG, Hajibeygi H (2019) Multiscale finite volume method for finite-volume-based simulation of poroelasticity. J Comput Phys 379:309–324. https://doi.org/10.1016/j.jcp.2018.11.039

Shokrollahzadeh Behbahani S, Hajibeygi H, Voskov DV, Jansen JD (2022) Smoothed embedded finite-volume method (sEFVM) for modeling contact mechanics in deformable faulted and fractured porous media. J Comput Phys. https://doi.org/10.1016/j.jcp.2022.111143

Segall P (1985) Stress and subsidence resulting from subsurface fluid withdrawal in the epicentral region of the 1983 Coalinga earthquake. J Geophys Res 90:6801–6816. https://doi.org/10.1029/JB090iB08p06801

Segall P (1989) Earthquakes triggered by fluid extraction. Geology 17:942–946. https://doi.org/10.1130/0091-7613(1989)017<0942:ETBFE>2.3.CO;2

Segall P (1992) Induced stresses due to fluid extraction from axisymmetric reservoirs. Pure Appl Geophys 139:535–560. https://doi.org/10.1007/BF00879950

Segall P (2010) Earthquake and Volcano Deformation. Princeton University Press, Princeton

Segall P, Fitzgerald SD (1998) A note on induced stress changes in hydrocarbon reservoirs and geothermal reservoirs. Tectonophysics 289:117–128. https://doi.org/10.1016/S0040-1951(97)00311-9

Segall P, Grasso JR, Mossop A (1994) Poroelastic stressing and induced seismicity near the Lacq gas field, southwestern France. J Geophys Res 99:15423–15438. https://doi.org/10.1029/94JB00989

Soltanzadeh H, Hawkes CD (2008) Semi-analytical models for stress change and fault reactivation induced by reservoir production and injection. J Petrol Sci Eng 60:71–85. https://doi.org/10.1016/j.petrol.2007.05.006

Simo JC, Laursen TA (1992) An augmented Lagrangian treatment of contact problems involving friction. Comput Struct 42(1):97–116. https://doi.org/10.1016/0045-7949(92)90540-G

Simo JC, Oliver J, Armero F (1993) An analysis of strong discontinuities induced by strain-softening in rate-independent inelastic solids. Comput Mech 12(5):277–296. https://doi.org/10.1007/BF00372173

Schultz R, Wang R, Gu YJ, Haug K, Atkinson G (2017) A seismological overview of the induced earthquakes in the Duvernay play near Fox Creek, Alberta. J Geophys Res Solid Earth 122(1):492–505. https://doi.org/10.1002/2016JB013570

Terekhov KM (2020) Cell-centered finite-volume method for heterogeneous anisotropic poromechanics problem. J Comput Appl Math. https://doi.org/10.1016/j.cam.2019.112357

Timoshenko SP, Goodier JN (1970) Theory of elasticity, 3rd edn. McGraw-Hill, New York

Tripuraneni SRT, Novikov A, Voskov D (2023) Nonlinear finite volume discretization of geomechanical problem. Int J Numer Anal Methods Geomech 47(12):2283–2303. https://doi.org/10.1002/nag.3580

Uenishi K, Rice JR (2003) Universal nucleation length for slip-weakening rupture instability under nonuniform loading. J Geophys Res Solid Earth 108:17–11714. https://doi.org/10.1029/2001JB001681

Van den Bogert PAJ (2015) Impact of various modelling options on the onset of fault slip and fault slip response using 2-dimensional finite-element modelling

Van den Bogert PAJ (2018) Depletion-induced fault slip and seismic rupture: 2D geomechanical models for the Groningen field, the Netherlands

Voort N, Vanclay F (2015) Social impacts of earthquakes caused by gas extraction in the province of Groningen, The Netherlands. Environ Impact Assess Rev 50:1–15. https://doi.org/10.1016/j.eiar.2014.08.008

Viesca RC, Garagash DI (2018) Numerical methods for coupled fracture problems. J Mech Phys Solids 113:13–34. https://doi.org/10.1016/j.jmps.2018.01.008

Van Thienen-Visser K, Breunese JN (2015) Induced seismicity of the Groningen gas field: history and recent developments. Lead Edge 34(6):664–671. https://doi.org/10.1190/tle34060664.1

Van Wees JD, Fokker P, Van Thienen-Visser K, Wassing B, Osinga S, Orlic B, Ghouri SA, Buijze L, Pluymaekers M (2017) Geomechanical models for induced seismicity in the Netherlands: inferences from simplified analytical, finite element and rupture model approaches. Neth J Geosci 96:183–202. https://doi.org/10.1017/njg.2017.38

Van Wees JD, Pluymaekers M, Osinga S, Fokker P, Van Thienen-Visser K, Orlic B, Wassing B, Hegen D, Candela T (2019) 3-D mechanical analysis of complex reservoirs: a novel mesh-free approach. Geophys J Int 219:1118–1130. https://doi.org/10.1093/gji/ggz352

Wang H (2000) Theory of linear poroelasticity with applications to geomechanics and hydrogeology. Princeton University Press, Princeton

Weertman J (1996) Dislocation based fracture mechanics. World Scientific, Singapore

Wu H, Vilarrasa V, De Simone S, Saaltink M, Parisio F (2021) Analytical solution to assess the induced seismicity potential of faults in pressurized and depleted reservoirs. J Geophys Res Solid Earth 126:2020–020436. https://doi.org/10.1029/2020JB020436

Wu H, Rutqvist J, Vilarrasa V (2024) Analytical solution to quickly assess ground displacement for a pressurized or depleted deep reservoir intersected by a fault in a half space. Int J Rock Mech Min Sci 174:105641. https://doi.org/10.1016/j.ijrmms.2024.105641

Xu F, Hajibeygi H, Sluys LJ (2021) Multiscale extended finite element method for deformable fractured porous media. J Comput Phys 436:110287. https://doi.org/10.1016/j.jcp.2021.110287

Yastrebov VA (2013) Numerical methods in contact mechanics. https://doi.org/10.1002/9781118647974